Supporting Information

Macro-micro Coordination Optimization of Lead Iodide Reactivity toward Millimeter-to-centimeter-scale Perovskite Solar Cells with Minimal Efficiency Loss

Yang Zhong,[a] Zhipeng Liu,[a] Xiao Luo,[a] Gengling Liu,[e] Xueying Wang,[a] Jiacheng He,[a] Wangping Sheng,[a] Dejian Yu,[f] Chao Liang,[g] Licheng Tan*[a,d] and Yiwang Chen*[a,b,c,d]

[a]College of Chemistry and Chemical Engineering/Film Energy Chemistry for Jiangxi Provincial Key Laboratory (FEC), Nanchang University, 999 Xuefu Avenue, Nanchang 330031, China

[b]Key Lab of Fluorine and Silicon for Energy Materials and Chemistry of Ministry of Education, Jiangxi Normal University, 99 Ziyang Avenue, Nanchang 330022, China

[c]College of Chemistry and Chemical Engineering, Gannan Normal University, Ganzhou 341000, China

[d]Peking University Yangtze Delta Insititute of Optoelectronics, Nantong 226010, China

[e]Key Laboratory of Bioinorganic and Synthetic Chemistry (MoE), Lehn Institute of Functional Materials, School of Chemistry, Sun Yat-sen University Guangzhou 510006, China

[f]Joint Key Laboratory of the Ministry of Education, Institute of Applied Physics and Materials Engineering, University of Macau, Taipa, Macao SAR 999078, China

[g]MOE Key Laboratory for Nonequilibrium Synthesis and Modulation of Condensed Matter, School of Physics, National Innovation Platform (Center) for Industry-Education Integration of Energy Storage Technology, Xi'an Jiaotong University, Xi'an 710049, China

Peking University Yangtze Delta Insititute of Optoelectronics, Nantong 226010, China

E-mail: ywchen@ncu.edu.cn (Y. C.); tanlicheng@ncu.edu.cn (L. T.)

Experimental Section

Materials and Reagents: N, N-dimethylformamide (DMF, 99.8% purity), dimethyl sulfoxide (DMSO, 99.9% purity), acetonitrile (99.8% purity), chlorobenzene (CB, 99.8% purity), 4-tert-butyl pyridine (tBP), Dihydrolevoglucosenone (Cyrene^{TM}, 98.5% purity) were purchased from Sigma-Aldrich and used as received without further purification. Tin(IV) oxide (SnO_2, 15% in H_2O colloidal dispersion liquid) and lithium bis(trifluoromethylsulfonyl) imide (Li-TFSI, >98% purity) were purchased from Alfa Aesar. Formamidinium iodide (FAI, 99.8%), methylamine iodide (MAI, 99.5%), methylamine hydrochloride (MACl, 99.5%) and poly[bis(4-phenyl)(2,4,6-trimethylphenyl)amine] (PTAA) were purchased from Xi'an Yuri Solar Co., Ltd. Lead iodide (PbI_2, 99.9985% purity), cesium iodide (CsI, 99.99% purity), 2,2',7,7'-Tetrakis [N, N-di(4-methoxyphenyl) amino]-9,9'-spirobifluorene (spiro-OMeTAD, 99% purity) was purchased from Advanced Election Technology Co., Ltd. Indium tin oxide (ITO) (transmission>95%) substrates were purchased from South China Science & Technology Company Limited. Polystyrene (PS) microsphere was purchased from KBsphere. Silver (Ag, 99.995%) has been purchased from ZhongNuo Advanced Material (Beijing) Technology Co., Ltd. Unless specified, all chemicals are employed as received without further modifications after purchase.

Device Fabrication: ITO-coated glass substrates were cleaned in an ultrasonic bath containing acetone, deionized (DI) water, and isopropanol (IPA) for 20 min in each step and then dried with a nitrogen (N_2) stream followed by air plasma treatment for 10 min. A uniform and dense SnO_2 layer was deposited onto an ITO substrate by spin-coating SnO_2 nanoparticle solution (Alfa Aesar, tin(IV) oxide, 15% in H_2O colloidal dispersion, SnO_2 colloidal solution/DI water, a ratio of 1:3) at 3000 rpm for 30 s, and annealed in ambient air at 150 °C for 30 min. It is better to clean the substrate with ultraviolet ozone for 10 min to improve the surface wetting. For pristine PbI_2 film, 50 μL of PbI_2 (1.5 M, DMF: DMSO = 95:5) was spin-coated onto SnO_2 at 1,500 rpm for 30 s, and annealed at 70 °C for 1 min, then cooled to room temperature. For the templated PbI_2 film, the PS

solution was spin-coated on the SnO_2 film at 1500-4500 rpm for 50 s to fabricated PS monolayer, then annealed at 80 °C for 30 min to obtain hydrophobic films. Then the films were treated by plasma for 3 minutes to enhance the surface hydrophily. Then, the PbI_2 solution was spin-coated fill into PS monolayer. After that, the films were dipped into toluene to wash large portion of PS content. For co-solvent strategy, different concentrations (1%, 3%, 5% v:v) Cyrene were additive into the PbI_2 solution. For $FAPbI_3$ perovskite film deposition, a solution of FAI: MAI: MACl (90 mg: 6.9 mg: 9 mg in 1ml IPA) was spin-coated onto the PbI_2 at 2000 rpm for 30 s, and the perovskite precursor film was taken out from the nitrogen glove box to ambient air for thermal annealing at 150 °C for 15 min in humidity conditions (30-40% humidity). For $MAPbI_3$ perovskite film deposition, a solution of MAI: MACl (60 mg: 9 mg in 1ml IPA) was spin-coated onto the PbI_2 at 1800 rpm. for 30 s, and the perovskite precursor film was taken out from the nitrogen glove box to ambient air for thermal annealing at 150 °C for 15 min in humidity conditions (30-40% humidity). After perovskite formation, the samples were transferred to a nitrogen-filled glove box for further processing. After cooling down, spiro-OMeTAD solution was spun with a ratio of 4000 rpm for 30 s. The spiro-OMeTAD solution was prepared by adding 72.3 mg spiro-OMeTAD in the solvent (CB 1 mL, 4-tertbutylpyridine 28.8 μL, Li-TFSI acetonitrile solution 17.5 μL, 520 mg mL^{-1}). Finally, ≈100 nm Ag was deposited through a shadow mask at a pressure of 7×10^{-4} Pa in a vacuum. The small device area was 0.04 cm^2. The centimeter-scale device area was 1.01 cm^2. All devices' measurements were carried out in drying cabinet at room temperature.

Module Fabrication: First, ITO on glass substrates were etched using a laser machine to form P1 lines. The substrates were cleaned sequentially with detergent, deionized water, and ethanol under ultrasonication for 15 min each. SnO_2 layer and perovskite layer were deposited via meniscus blade coating. After deposition of the Spiro-OMeTAD layer, the samples were re-etched to form P2 lines, and the Ag was etched to form P3 lines, creating series-connected modules.

Characterizations: Keithley 2400 was used to characterize the current density-voltage (*J-V*) curves. The currents were measured under 100 mW·cm^{-2} simulated AM 1.5 G irradiation (Abet5 Solar Simulator Sun2000). The standard silicon solar cell was corrected from NREL and the currents were detected under the solar simulator (Enli Tech, 100 mW cm^{-2}, AM 1.5 G irradiation). The forward scan range is from 0 V to 1.22 V and the reverse scan range is from 1.22 V to 0 V, with 20 mV for each step. The scan rate for the *J-V* measurement is 0.2 V/s. Devices were stored and tested in the nitrogen-filled glovebox. Scanning electron microscopy (SEM) was conducted on SU8020 scanning electron microscope operated at an acceleration voltage of 5 kV. The High-resolution transmission electron microscopy (HRTEM) were conducted on JEOL JEM-F200. Atomic force microscopy (AFM) images were measured by MultiMode 8- HR (Bruker) atomic force microscope. Microscopy photographs were conducted by WD-B106LX-B (Welldu). The ^{1}H nuclear magnetic resonance (^{1}H-NMR) spectrum was conducted by BRUKER/AVANCE NEO 300. X-ray diffraction (XRD) spectra were carried out by using X-ray diffractometer (Bruker D8Discover 25). The 2D GIXRD were conducted by using Xeuss 2.0/Pilatus 300K (Xenocs). The ultraviolet-visible (UV-Vis) spectra were characterized on UV-2600 spectrophotometer (Agilent Technologies Inc. Cary 5000 spectrophotometer). The Fourier-transform infrared (FTIR) spectra were conducted on Shimadzu IRAffinity-1S and Thermo Scientific Nicolet iS20. The steady-state photoluminescence (PL) spectra were recorded by fluorescence spectrophotometer (Hitachi F-7000) and time-resolved photoluminescence (TRPL) spectra were recorded by an Edinburgh instruments FLS920 spectrometer (Edinburgh Instruments Ltd.). The PL mapping images were conducted by FastFLIM Q2 (ISS Inc.). X-ray photoelectron spectroscopy (XPS, Thermo Scientific ESCALAB 250Xi) was used for binding energy and element distribution analysis. Thermogravimetric (TGA) were characterized by Discovery TGA55 (Waters). Electrical impedance spectroscopy (EIS) of the devices was performed in a frequency range from 1 MHz to 10 MHz using Zahner electrochemical workstation at an applied bias equivalent to the open-circuit voltage of the cell under 1 sun illumination. The water contact angle has been recorded at a Krüss DSA100s drop shape analyzer.

External quantum efficiency (EQE) values were measured under monochromatic illumination (Oriel Cornerstone 260 1/4 m monochromator equipped with an Oriel 70613NS QTH lamp), and the calibration of the incident light was performed using a monocrystalline silicon diode. Nanomeasurer 1.2 software were used for statistical analysis of size distributions.

Stability measurement: For all stability tests, the $FAPbI_3$ perovskite was used as the absorber. For light soaking stability test, unencapsulated PVSCs (5 devices for each condition) were exposed under 1-sun intensity continuous white LED illumination (AM 1.5G) in air (25±5 °C, 50±5% RH). Then the *J-V* curves of the unencapsulated PVSCs were recorded at different times and the corresponding photographs of the champion PVSC were captured. Additionally, cross-sectional SEM images of the devices were obtained both before and after aging during the light soaking process in ambient air. For continuous operational stability test, the *J-V* curves were recorded first to verify the voltage at the maximum power point (MPP). Then the operational stability tests were carried out at the MPP for unencapsulated devices under 1-sun intensity continuous white LED illumination (N_2 atmosphere). Note that during the whole MPP tracking, the illumination was continuously applied on the PVSCs except for the calibration of light source. For thermal stability test, unencapsulated PVSCs (5 devices for each condition) were exposed to a temperature at 85 °C in N_2 glove box. Moreover, considering that the Spiro-OMeTAD was not a stable HTL, we have replaced it with PTAA for improved stability under combined heat and light stressors. PTAA was used at a concentration of 15 mg/mL in chlorobenzene, with additives of 7.5 μL Li-TFSI/acetonitrile (180 mg/mL) and 10 μL 4-tert-butylpyridine, and spin-coated at 3000 rpm for 30 s. In addition, the unencapsulated PVSCs (5 devices for each condition) were exposed at 85 °C under AM 1.5G light soaking in N_2 atmosphere, following ISOS-L-2 standard..

Finite element analysis: The finite element analysis was performed on COMSOL Multiphysics 6.0 using the following equation: $\frac{\partial c_i}{\partial t} + \nabla \cdot J_i + u \cdot \nabla c_i = R_i$, $J_i = -D_i \nabla c_i$, where c_i is the concentration, t is the diffusion time, J_i is the diffusion flux, u is the velocity, and D_i is the diffusion coefficient. The physical meshes of TP-PbI_2 and NM-PbI_2 films were sampled using a tetragonal boundary with a

size of 8×8×0.6 μm^3. The surface FAI concentration of all structures are 90 mg/mL. The physical meshes of other materials were also sampled with a real thickness. The simulation graph depicts the FAI concentration of TP-PbI_2 and NM-PbI_2 films as a function of time.

Density Functional Theory (DFT) Calculations: We have used the Gaussian 09W program package to perform electronic structure calculations for binding energies. All calculations have been carried out at the level of DFT with the Becke-Lee Yang Parr (B3LYP) hybrid functional.

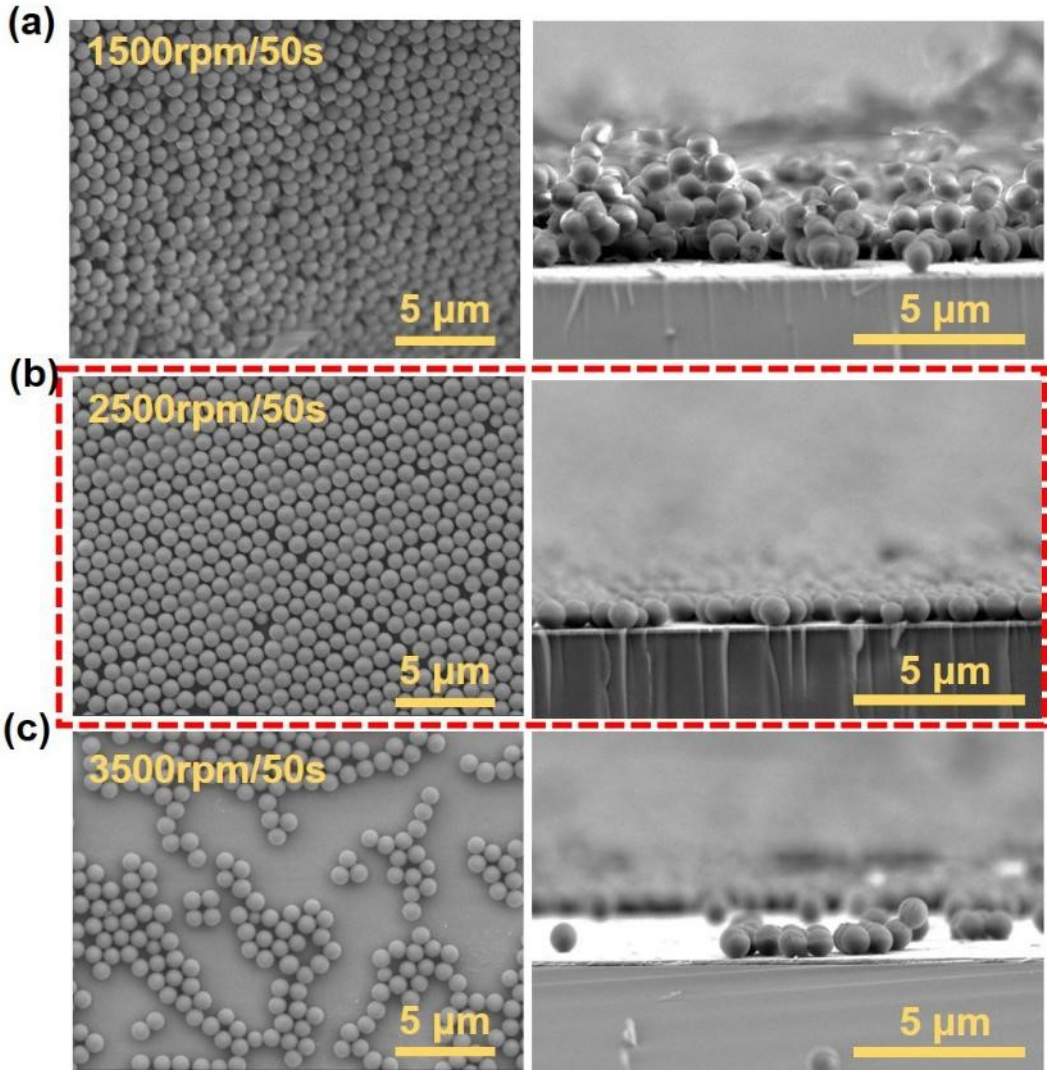

Fig. S1. (a-c) Top view SEM and corresponding cross-section SEM images of 1 μm diameter PS microspheres with different spin rates.

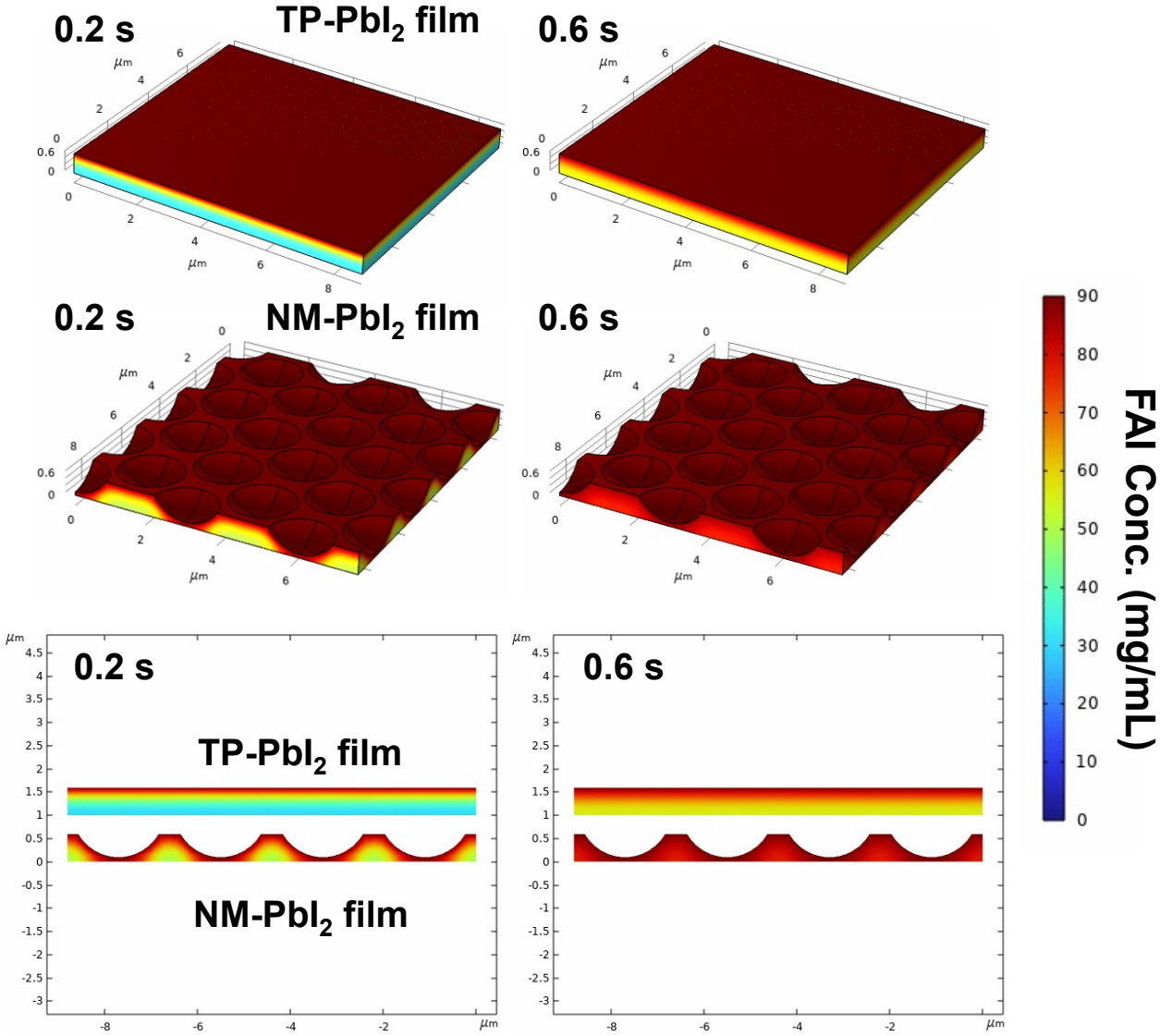

Fig. S2. (a, b) Finite element analysis of cross-section on the FAI concentration distribution for TP-PbI_2 and NM-PbI_2 films with diffusion time.

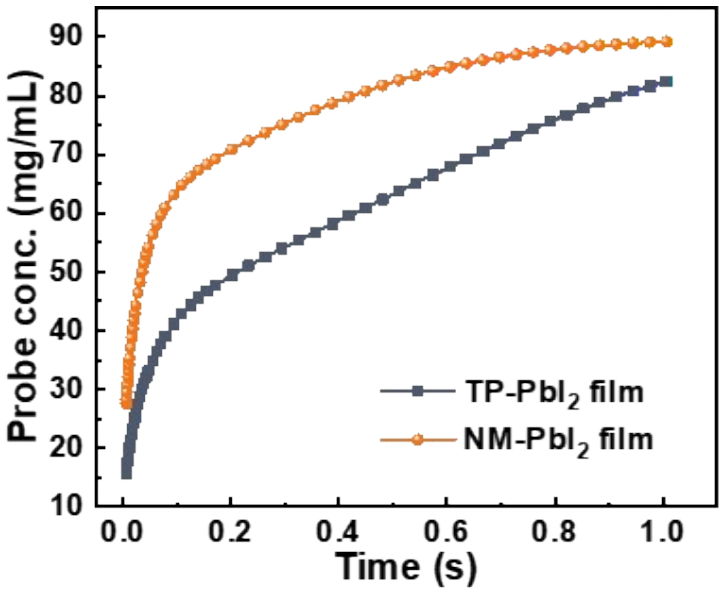

Fig. S3. FAI concentration evolution of TP-PbI_2 and NM-PbI_2 films with diffusion time.

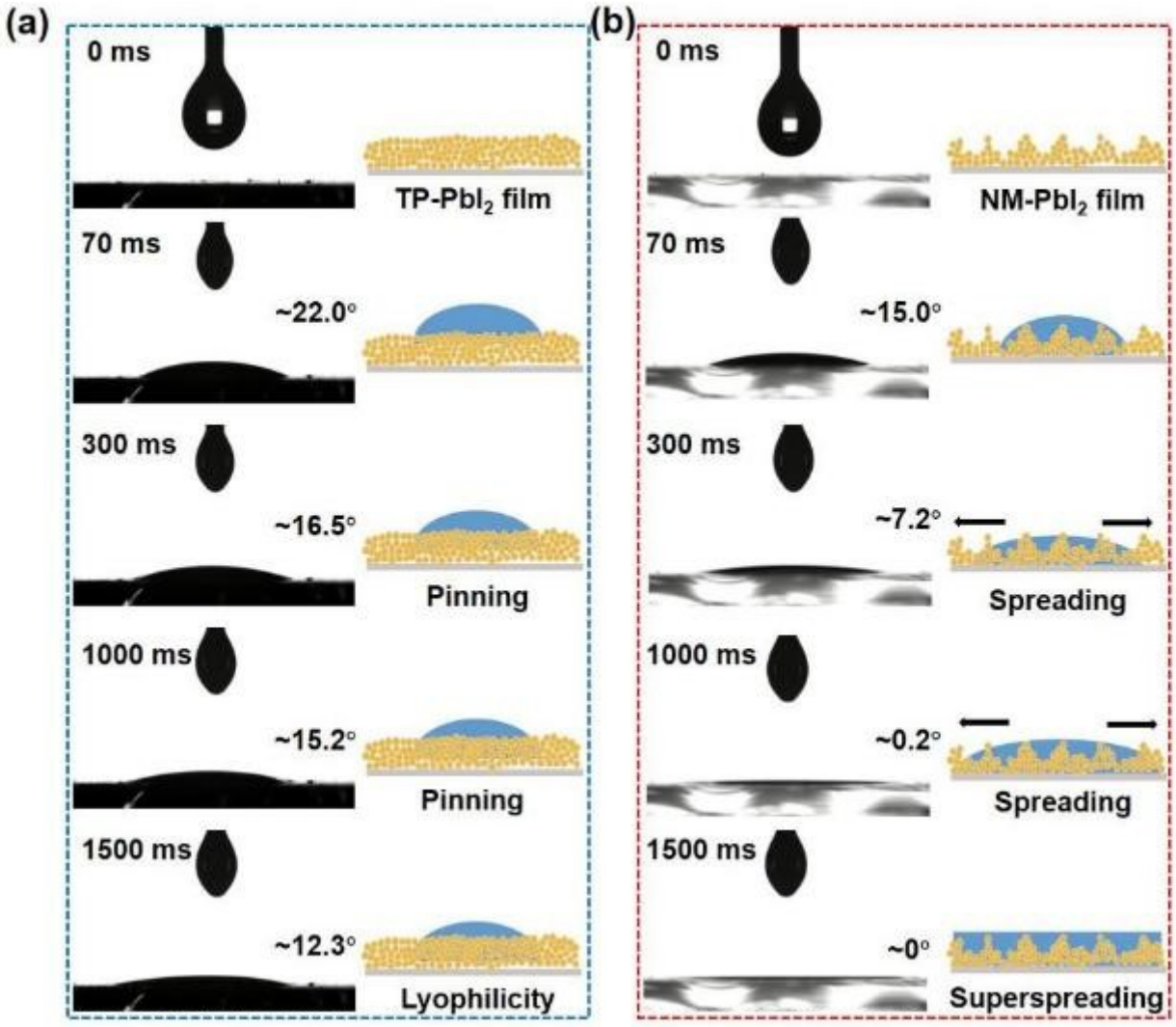

Fig. S4. Contact angle snapshots and schematics showing the dynamic spreading processes on (a) TP-PbI_2 film and (b) NM-PbI_2 film. On NM-PbI_2 film, liquids can completely spread out until the contact angle approaches nearly 0°, while the contact angle on dense PbI_2 film is ≈12.3°.

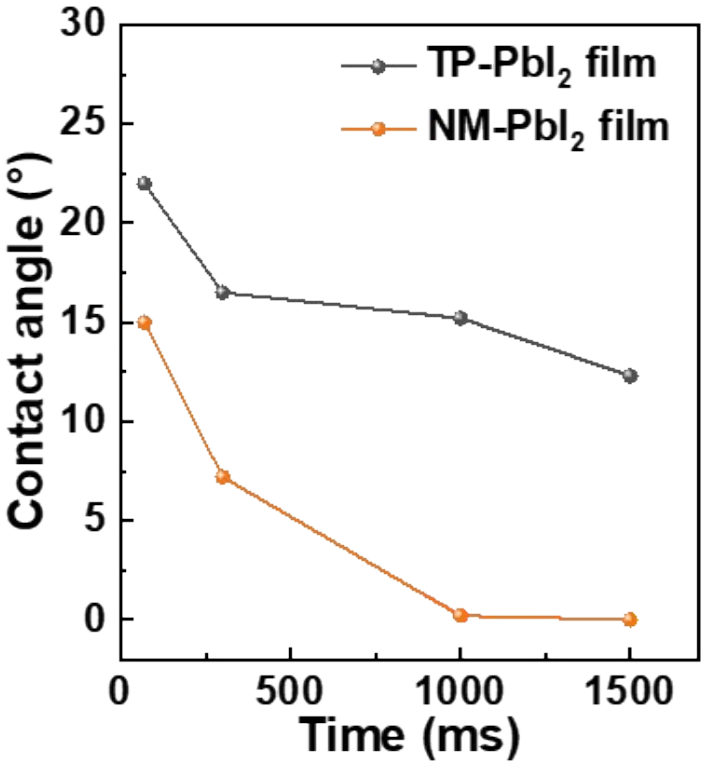

Fig. S5. Variation in contact angle on TP-PbI_2 film and NM-PbI_2 film as a function of time.

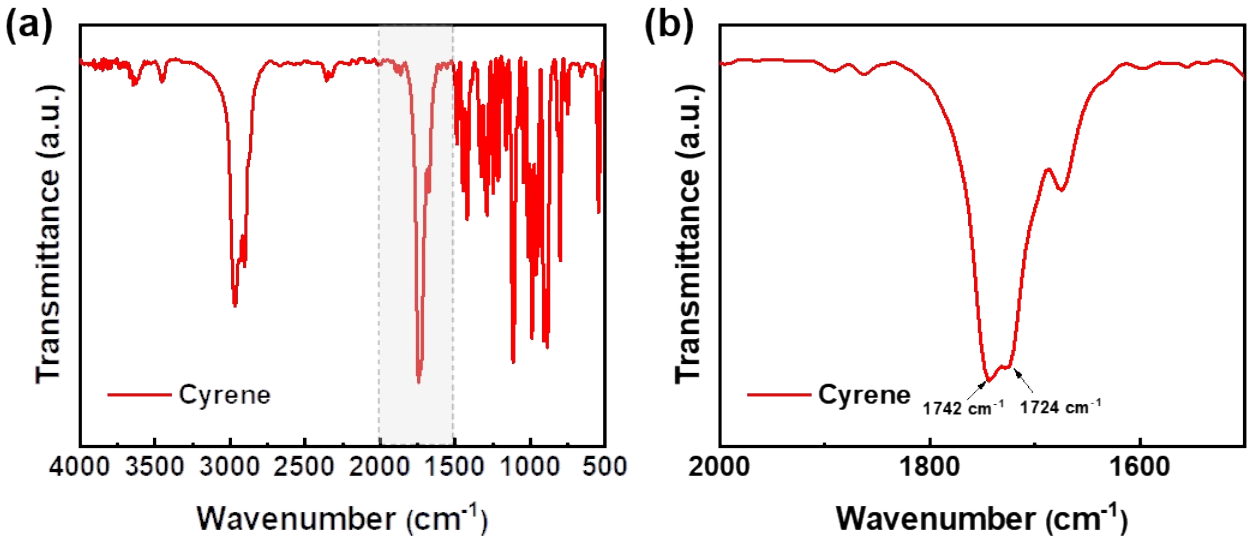

Fig. S6. FTIR spectra of and fingerprint regions for C=O stretching vibrations from pure Cyrene.

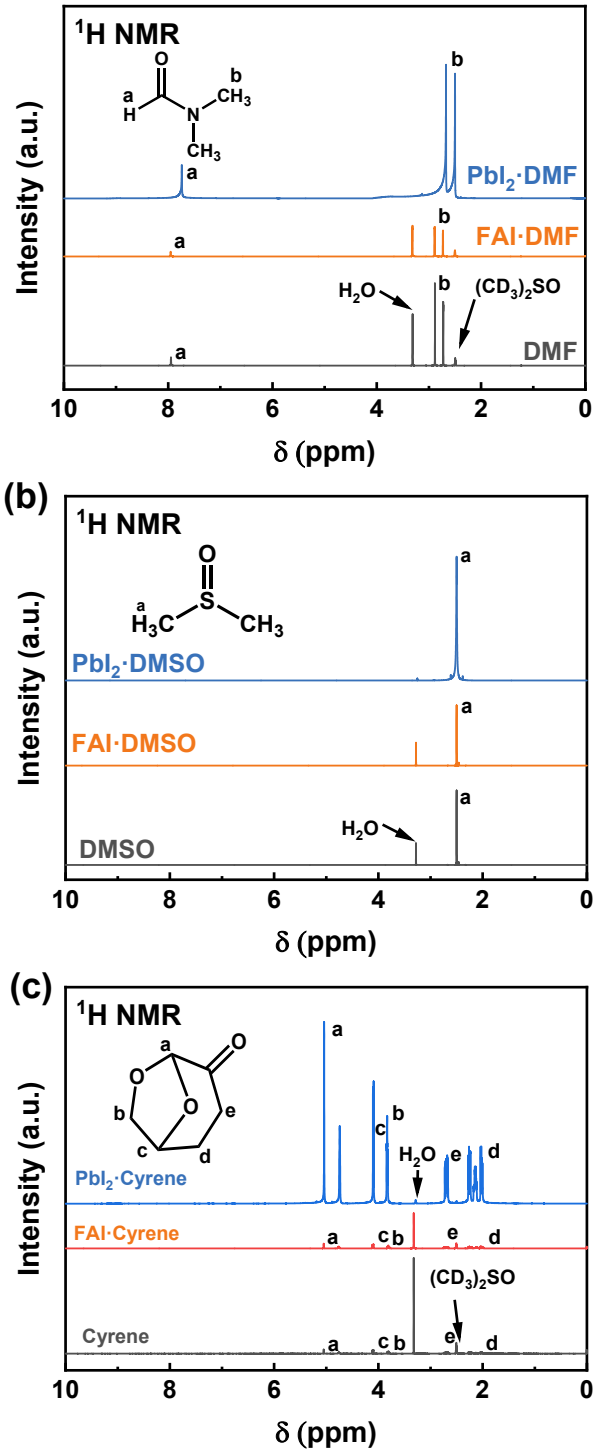

Fig. S7. ^{1}H NMR spectra of FAI and PbI_2 precursors in (a) DMF, (b) DMSO and (c) Cyrene, respectively. It can be observed that the a-H peak of Cyrene at 5.05 parts per million (ppm) shifts to the lower value of 5.04 ppm after introducing Cyrene, indicating a chemical interaction between PbI_2 and Cyrene existed due to the formation of adducts. Moreover, the FAI·Cyrene exhibits below 0.02 ppm indicate that the strong hydrogen bonding of C=O···H-N affects the electron cloud density of a-H.

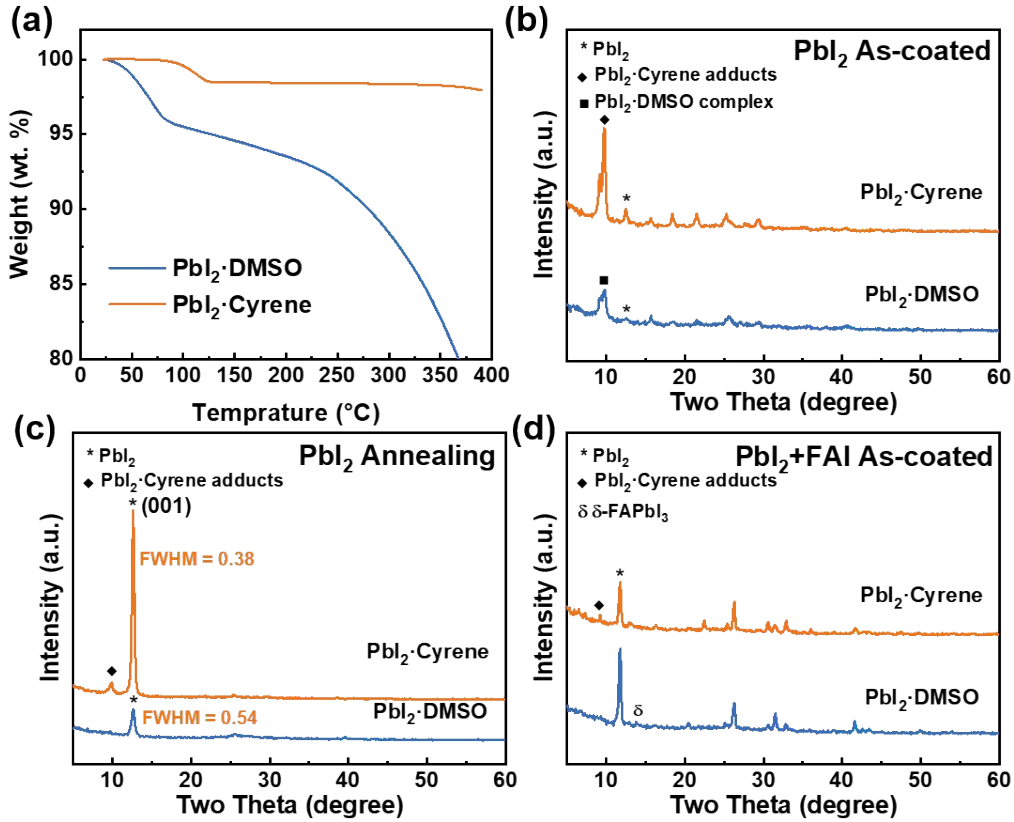

Fig. S8. (a) Thermogravimetric (TGA) analysis of different PbI_2·solvent complexes. XRD patterns of (b) as-coated PbI_2 films, (c) annealing PbI_2 films, and (d) as-coated PbI_2+FAI films based PbI_2·solvent complexes. The different PbI_2·solvent complexes have been estimated by thermogravimetric analysis (TGA) (Figure S7a). Weight loss at a relatively low temperature (<250 °C) can be attributed to evaporation of DMSO or Cyrene. The PbI_2·DMSO adduct powder shows two distinct weight losses at around 70 and 230 °C. However, PbI_2·Cyrene adduct powder shows single weight loss at around 120 °C, which indicates that the PbI_2·Cyrene adduct is more stable, which corresponds to the previous conclusion. Moreover, we have further confirmed the formation of this adduction by XRD. As shown in Figure S7b, the diffraction peak of PbI_2·Cyrene is higher than the PbI_2·DMSO complex in as-coated wet PbI_2 film. As shown in XRD pattern for PbI_2·Cyrene as-coated film, the peak is consistent with that of the PbI_2·Cyrene complex powder, although its crystallinity was lower. When PbI_2 films annealing, the film based PbI_2·Cyrene produces a very strong PbI_2 crystallization peak with intermediate adducts (Figure S7c), indicating PbI_2·Cyrene adduct is more stable. When the FAI solution is coated on the annealed PbI_2 film, the highly active and highly oriented PbI_2 film with Cyrene accelerates the transformation to the perovskite phase (**Figure S8d, S9**), which is also consistent with our previous conclusions.

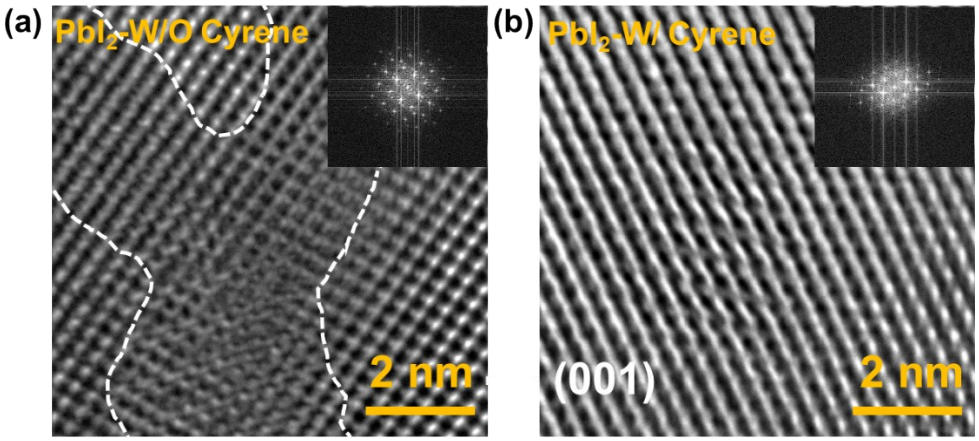

Fig. S9. High-resolution transmission electron microscopy (HRTEM) and Fourier transform of PbI_2 films with or without Cyrene. Moreover, we have found the random orientation of PbI_2 film without cosolvent Cyrene from the HRTEM (Figure S9a), whereas the (001)-oriented PbI_2 domains have a high degree of orientation and show a very regular arrangement in the PbI_2 film with Cyrene (Figure S9b). This indicates that the introduction of the cosolvent Cyrene makes the PbI_2 film have a highly vertical orientation, which helps to form a nanoscale ion channel between the layered PbI_2, and provides a direct channel for the exchange reaction between the cation and the solvent molecule.

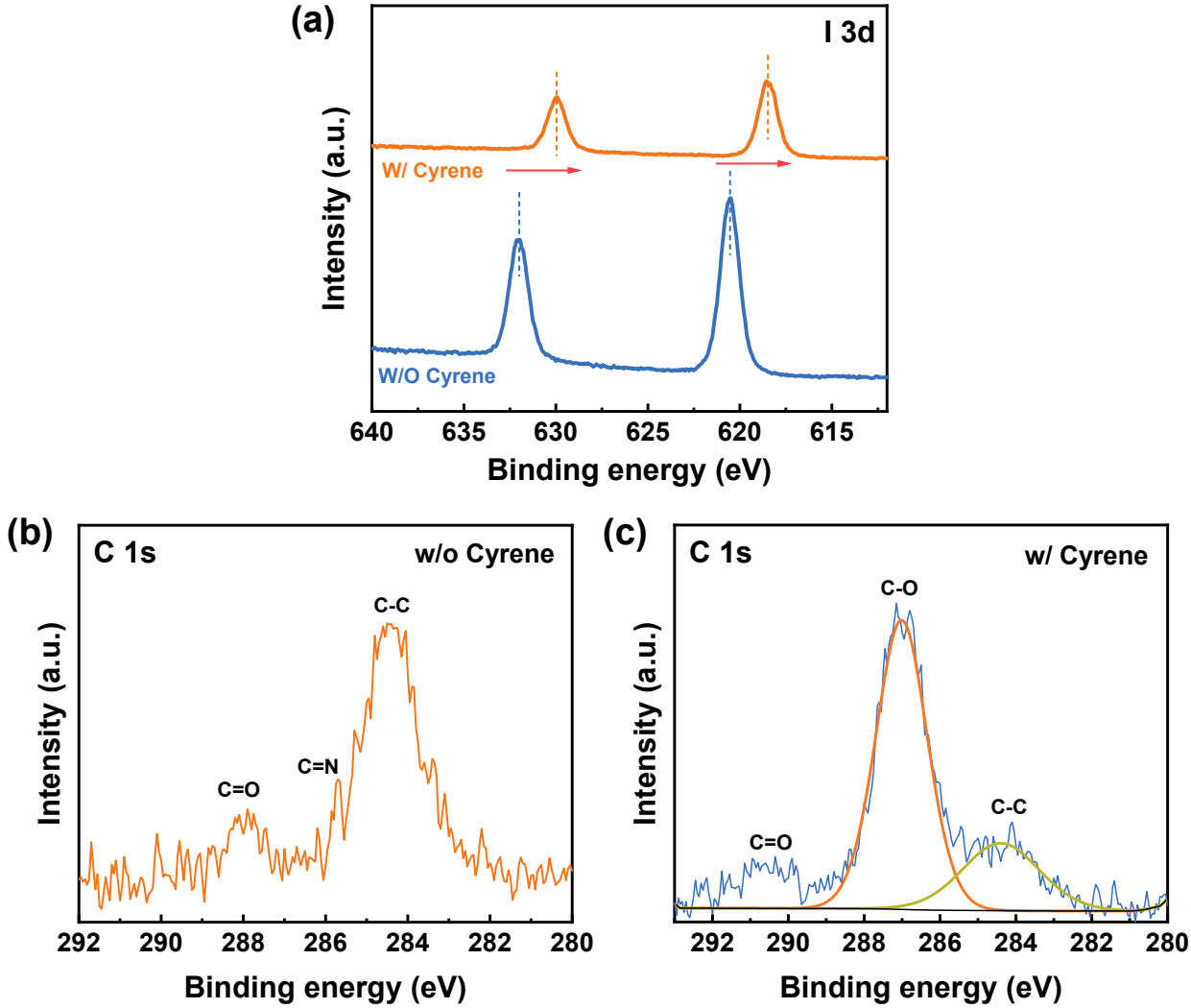

Fig. S10. XPS of (a) Pb 4f, (b) I 3d and (c) C 1s of perovskites with and without Cyrene.

Fig. S11. The photograph of PbI_2 solutions with different content of Cyrene (without, with 1%, 3% and 5%) and Cyrene solution.

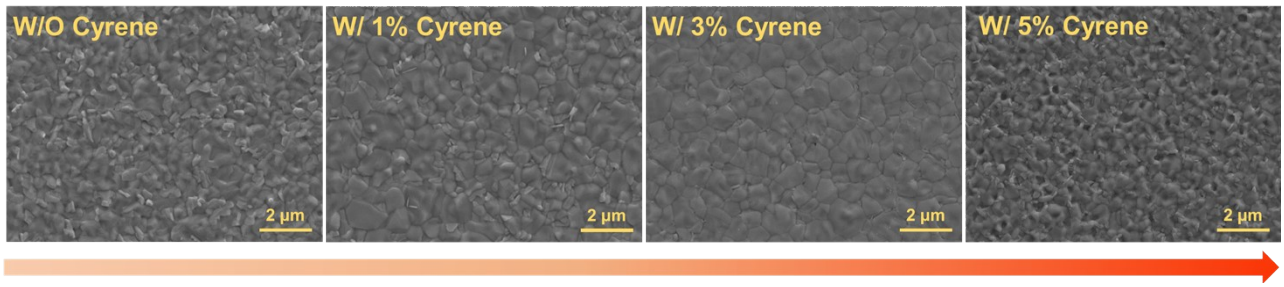

Fig. S12. SEM images of perovskite films with different content of Cyrene (without, with 1%, 3% and 5%).

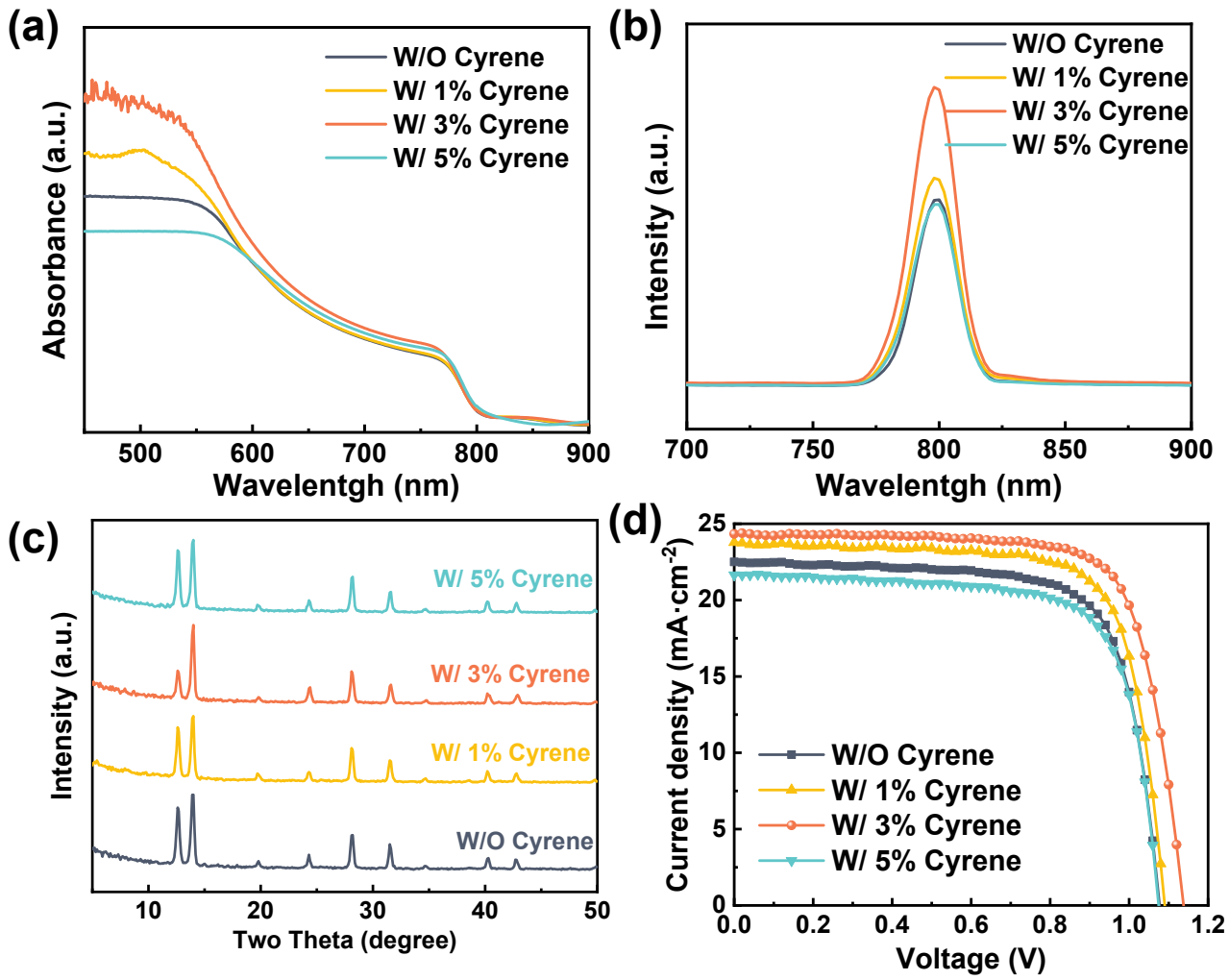

Fig. S13. (a) UV-vis absorption and (b) PL spectra, and (c) XRD patterns of perovskite films with different content of Cyrene (without, with 1%, 3% and 5%). (d) *J-V* curves of 1.01 cm^2 PVSCs based on perovskite films with different content of Cyrene (without, with 1%, 3% and 5%) under AM 1.5G 100 mW/cm^2 illumination.

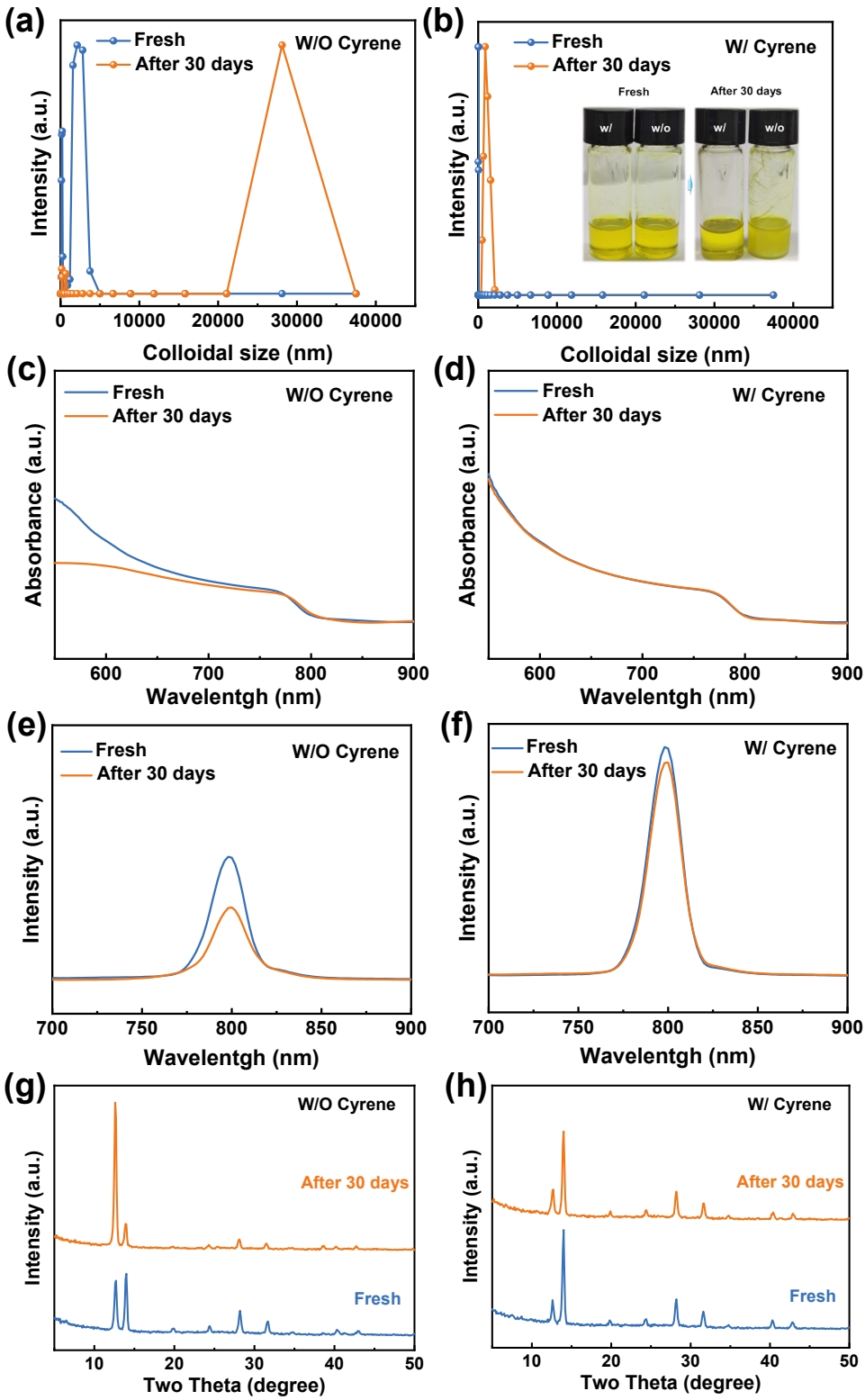

Fig. S14. (a, b) DLS spectra of PbI_2 precursor ink (a) with or (b) without Cyrene aging after 30 days in air at 25±5 °C with RH of 50±5%. The insets in (b) show the corresponding PbI_2 precursor ink photographs. (c, d) UV-vis absorption spectra, (e, f) PL spectra, (g, h) XRD patterns of perovskite films based on PbI_2 precursor ink with or without Cyrene aging after 30 days in air at 25±5 °C with RH of 50±5%.

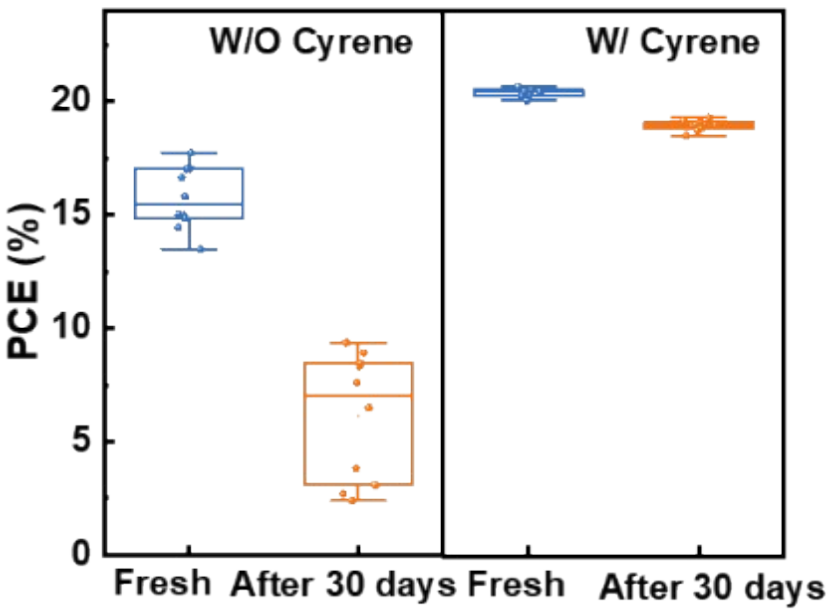

Fig. S15. PCE distribution of PVSCs based on PbI_2 precursor ink with or without Cyrene aging after 30 days.

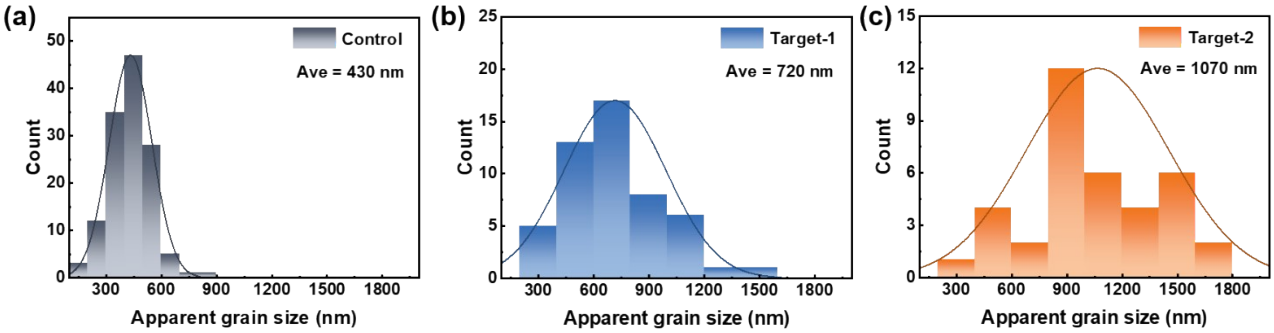

Fig. S16. Apparent grain size distributions calculated from top-view SEM images of control, target-1 and target-2 perovskite films using the Nanomeasurer 1.2 software.

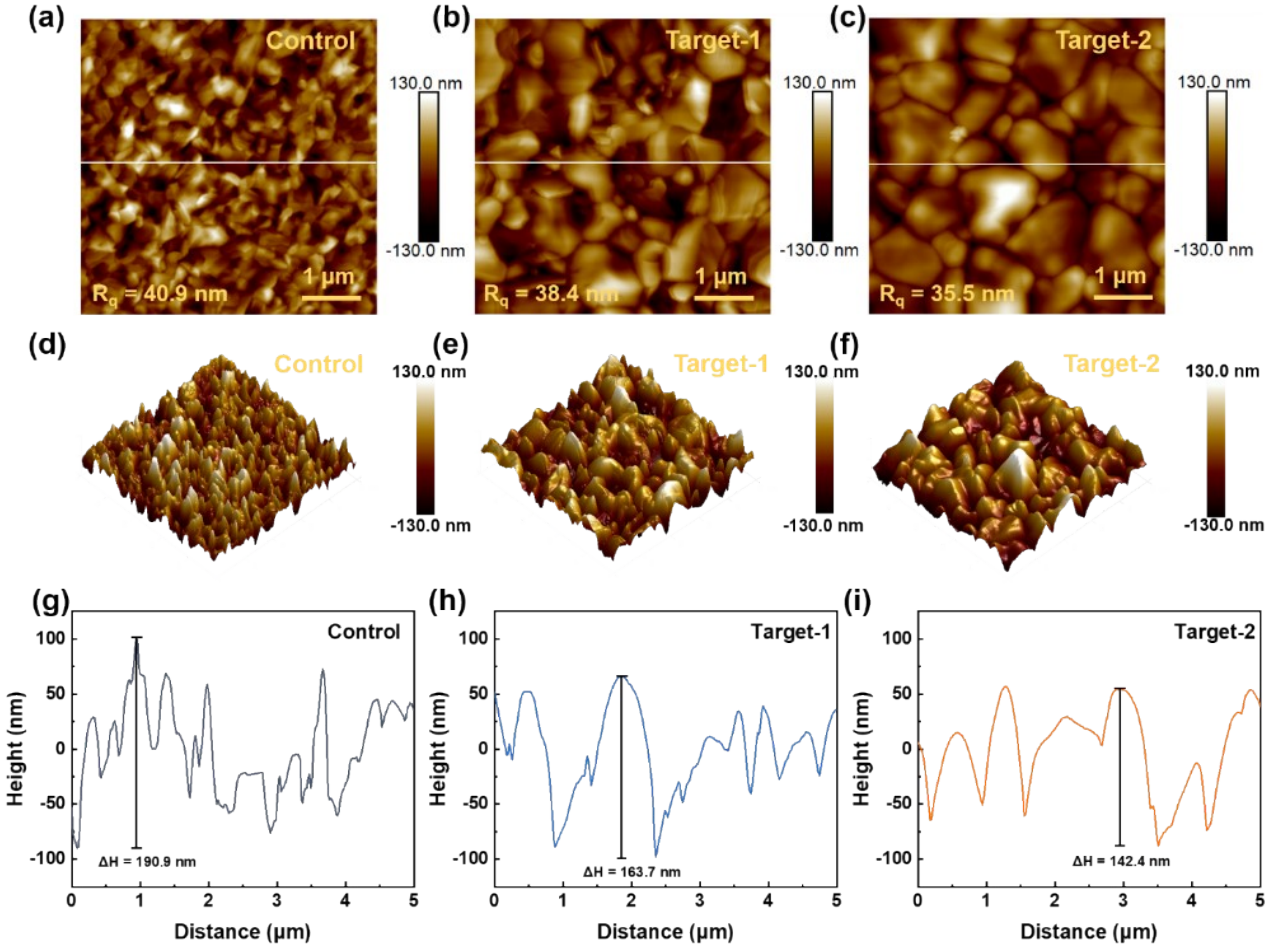

Fig. S17. (a-c) AFM height images, (d-f) corresponding 3D height images and (g-i) height variation along the lines of control, target-1 and target-2 perovskite films, respectively. For the control perovskite film, the perovskite surface morphology shows a small crystal size and a relatively high root mean square roughness (R_q) of 40.9 nm (Figure S14a, d). By further analyzing the height variation (Figure S14g), it can be found that the control film exhibits obvious height difference (ΔH = 190.9 nm). The perovskite surface morphology of target-1 film shows a larger crystal size and lower R_q (38.4 nm) with lower height difference (163.7 nm) (Figure S14b, e, d). Compared with the control and target-1, the target-2 perovskite surface morphology exhibits a largest crystal size and lowest R_q (35.5 nm) with lower height difference of 142.4 nm (Figure S14c, f, i), which indicates the film has a flat and dense morphology with superior crystal quality.

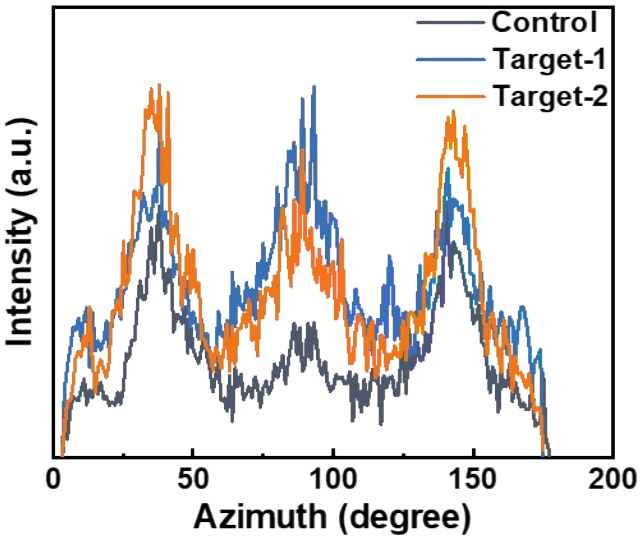

Fig. S18. Radially integrated intensity plots along the ring at q = 1.0 $Å^{-1}$ of control, target-1 and target-2 perovskite films, respectively. As there is rotational isotropy around the substrate normal, the scattering is symmetric in azimuthal angle. The distribution from 0° to 90° gives the full information of the orientation distributions, while the patterns between 90° and 180° reflect the symmetric diffractions. In the control film, the 2D GIXRD pattern shows an isotropic intensity distribution along the azimuthal angle, indicating random orientation of perovskite crystals. The target-1 and target-2 film at an azimuthal angle of 30° is significantly surpass that of the control film, while the target-1 film at the azimuthal angle roughly around at 90° displays a relative a stronger than target-2 film, which demonstrate that the target-2 film exhibits an emerging preferable orientation along the perpendicular direction. The orientational distribution and orientational degree may play crucial roles in managing the structural and optoelectronic properties of perovskite film.

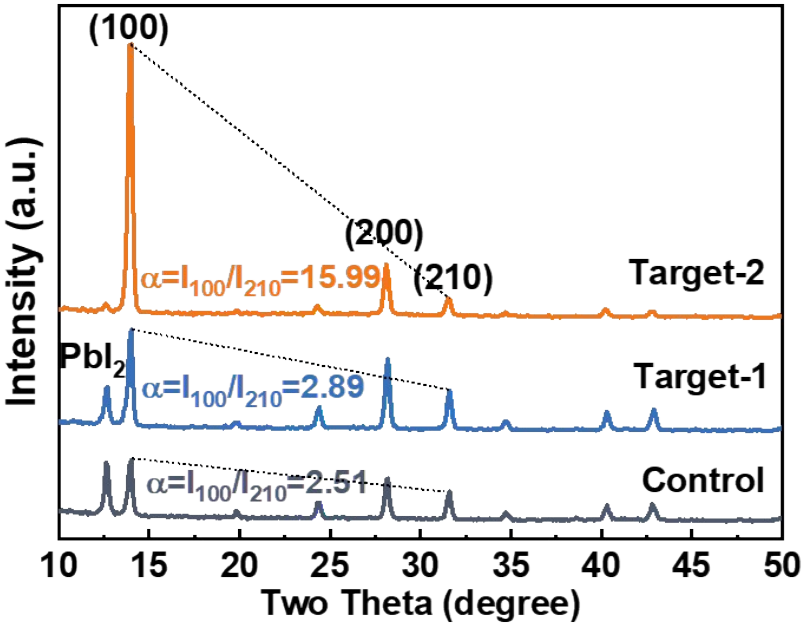

Fig. S19. XRD patterns of control, target-1 and target-2 perovskite films, respectively.

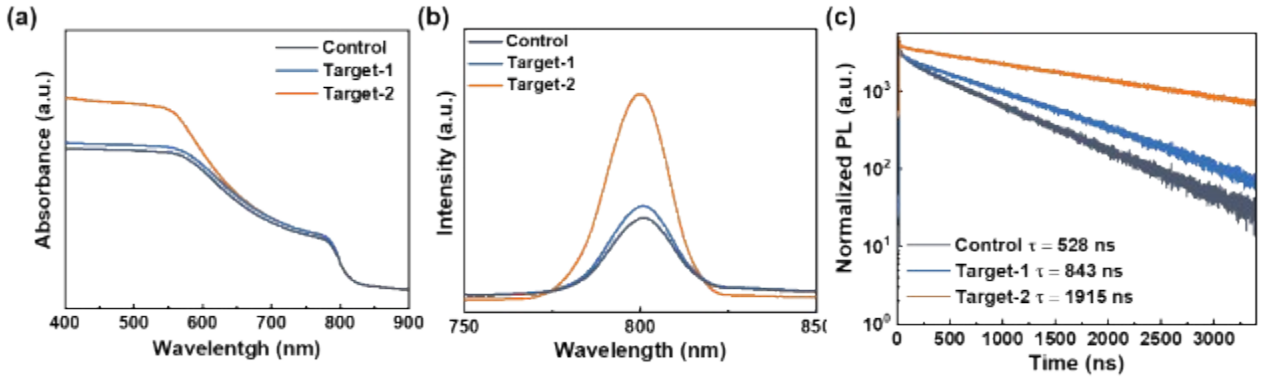

Fig. S20. (a) UV-vis absorption, (b) PL and (c) TRPL spectra for control, target-1 and target-2 perovskite films, respectively.

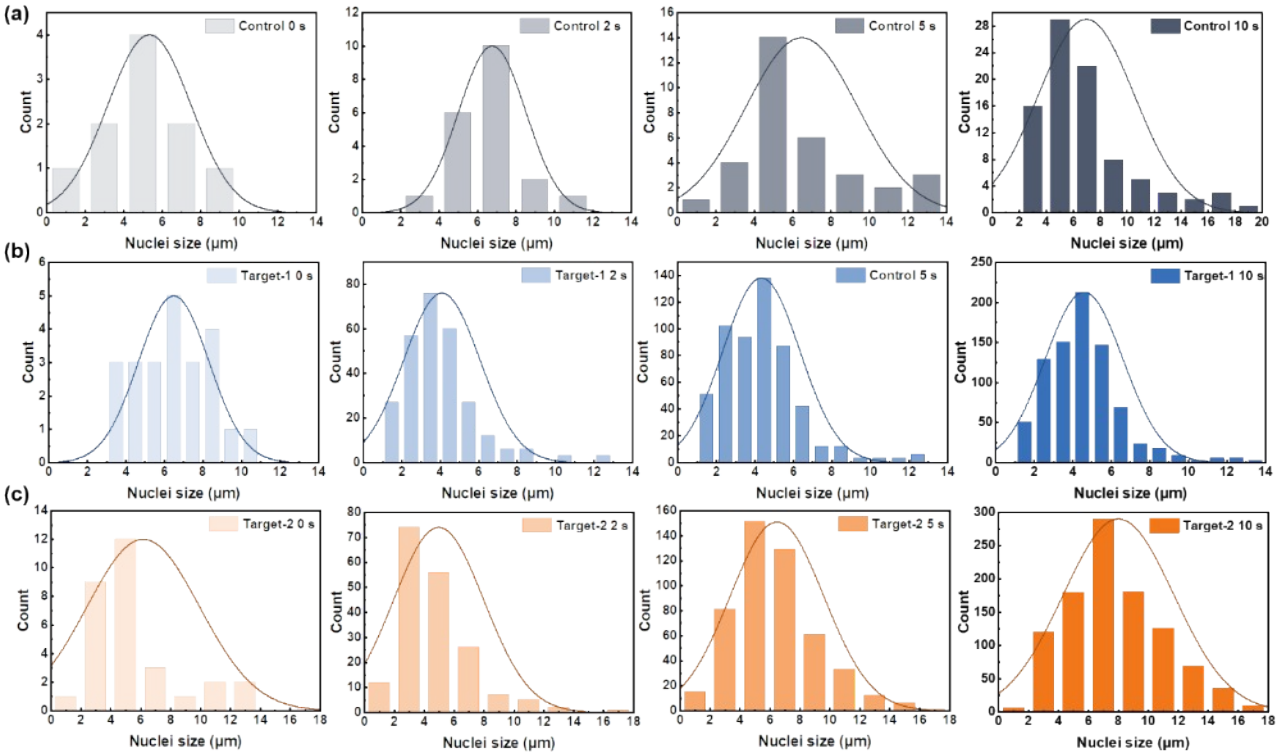

Fig. S21. Nuclei size distributions calculated from microscopy photographs of evolutions of (a) control, (b) target-1, and (c) target-2 PbI_2 films at different reaction times after depositing organic salts using the Nanomeasurer 1.2 software.

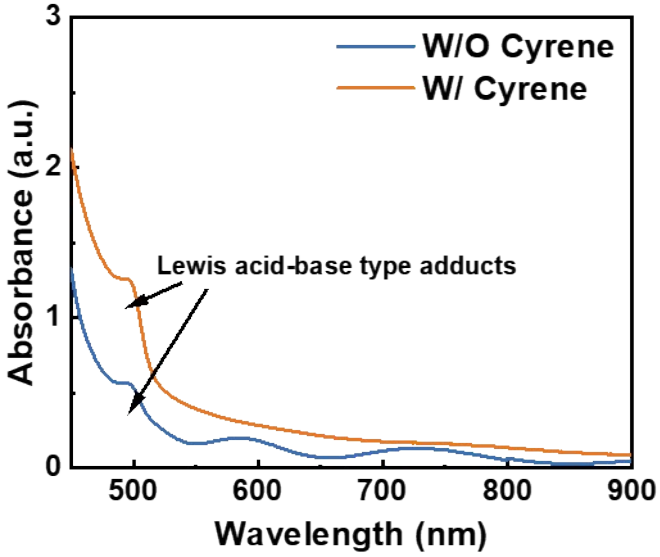

Fig. S22. UV-vis absorption spectra of PbI_2 films with or without Cyrene.

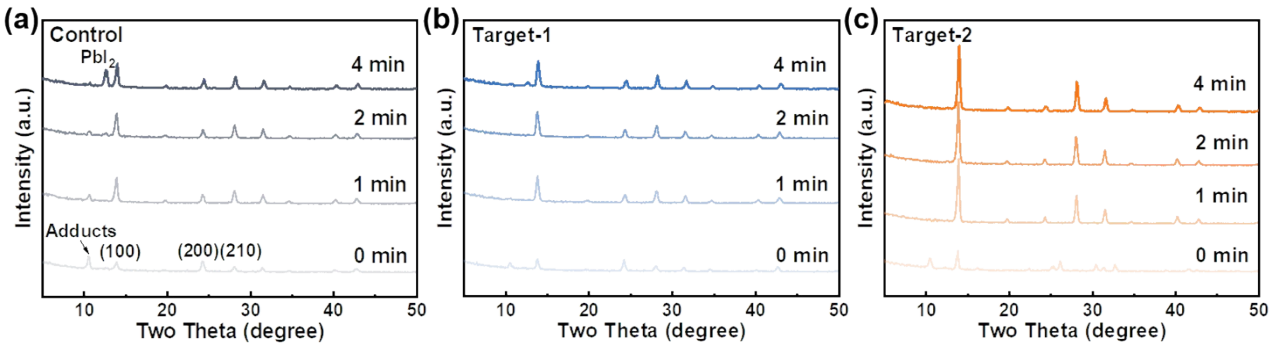

Fig. S23. XRD patterns during the annealing process with varied time (0, 1, 2 and 4 min) at an incident angle of 1.0° for (a) control, (b) target-1 and (c) target-2, respectively. At 1 min and 2 min of annealing, the characteristic diffraction peaks of PbI_2 are absent, suggesting that PbI_2 existed primarily in a solvated amorphous phase during these shorter annealing periods. At 4 min of annealing, we observe the emergence of PbI_2 characteristic diffraction peaks in both control and target-1 films, indicating the gradual transformation of PbI_2 from the amorphous phase to the crystalline phase. These results clearly demonstrate the transition of PbI_2 from an amorphous to a crystalline state during the annealing process, supporting a diffusion-limited conversion mechanism. However, in the target-2 sample, the solvated amorphous phase can be rapidly transformed into the optically active perovskite phase directly within just 1 min, indicating that the macro-micro synergistic strategy facilitates sufficient diffusion while promoting phase transition.

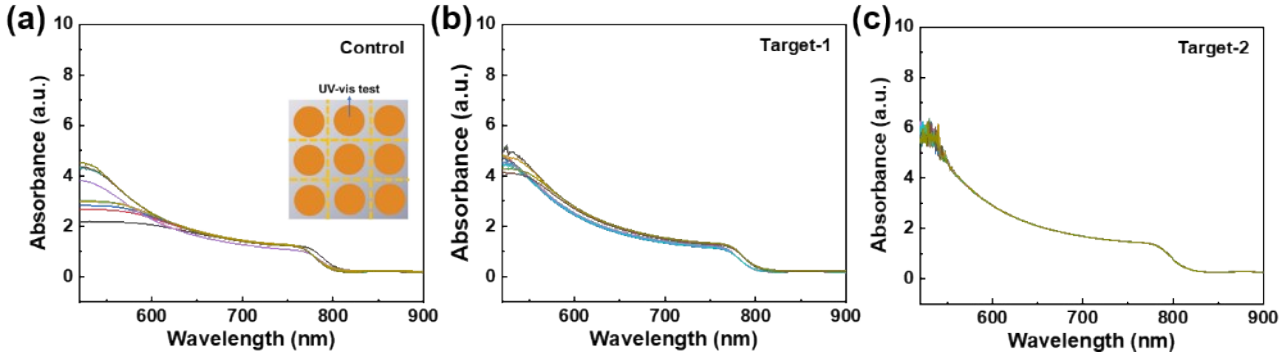

Fig. S24. UV-vis absorption of 9 different points in 2.5×2.5 cm^2 specimen of (a) control, (b) target-1 and (c) target-2 perovskite films, respectively. The insets show the schematic illustration of UV-vis test sites.

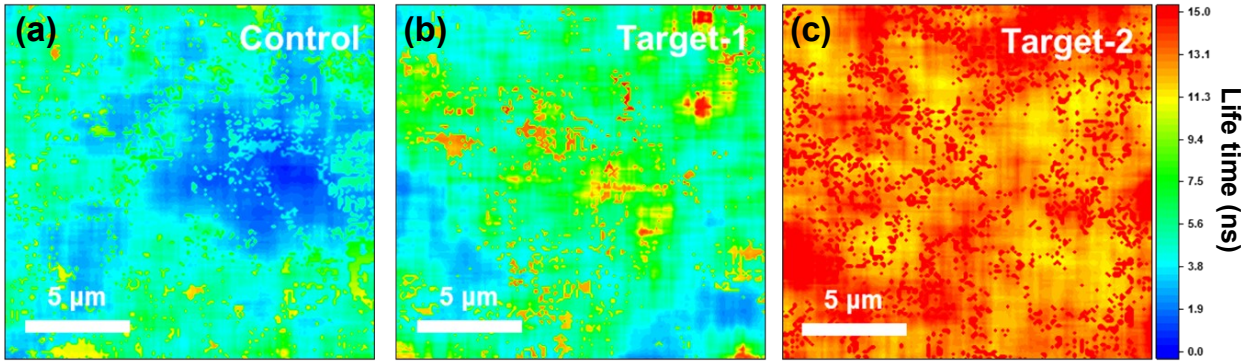

Fig. S25. TRPL mapping images of (a) control, (b) target-1 and (c) target-2 perovskite films, respectively.

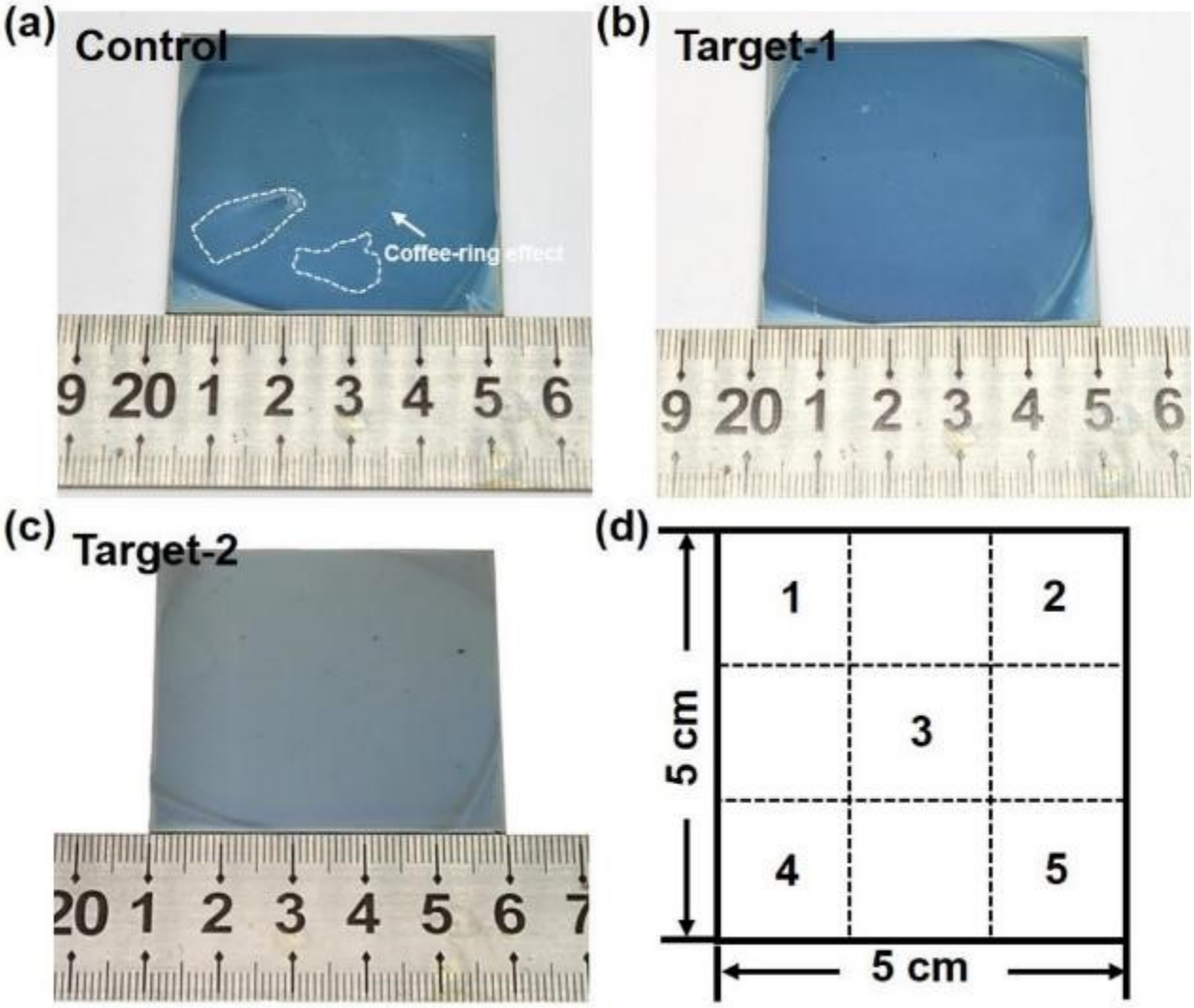

Fig. S26. Photographs of 5×5 cm^2 area for (a) control, (b) target-1 and (c) target-2 perovskite films, respectively. (d) Schematic illustration of the fabricated large-area perovskite films which cut into 5 select pieces (regions 1-5).

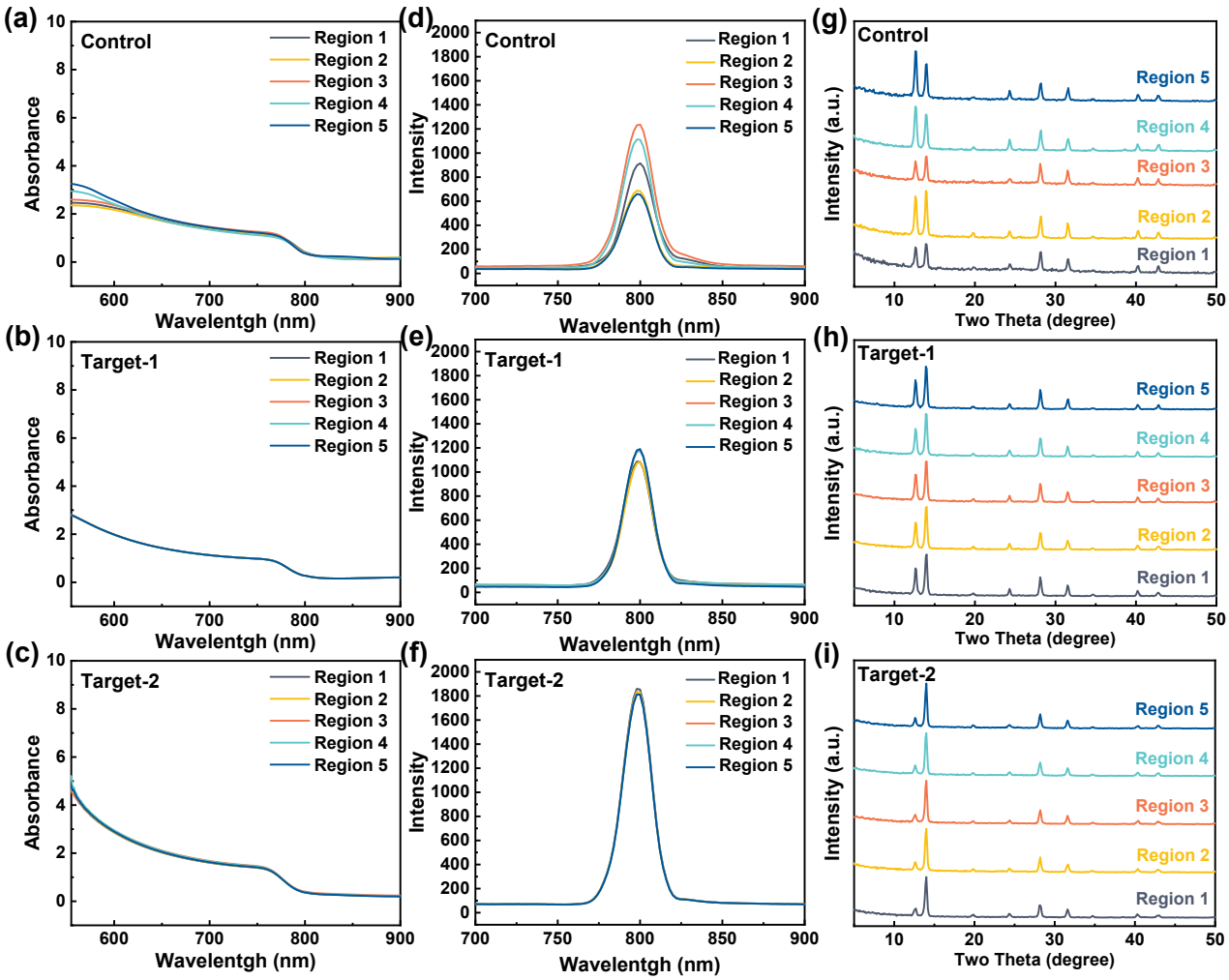

Fig. S27. (a-c) UV-vis absorption spectra, (d-f) PL spectra and (g-i) XRD patterns of 5 select pieces (regions 1-5) from large area (5×5 cm^2) control, target-1 and target-2 perovskite films.

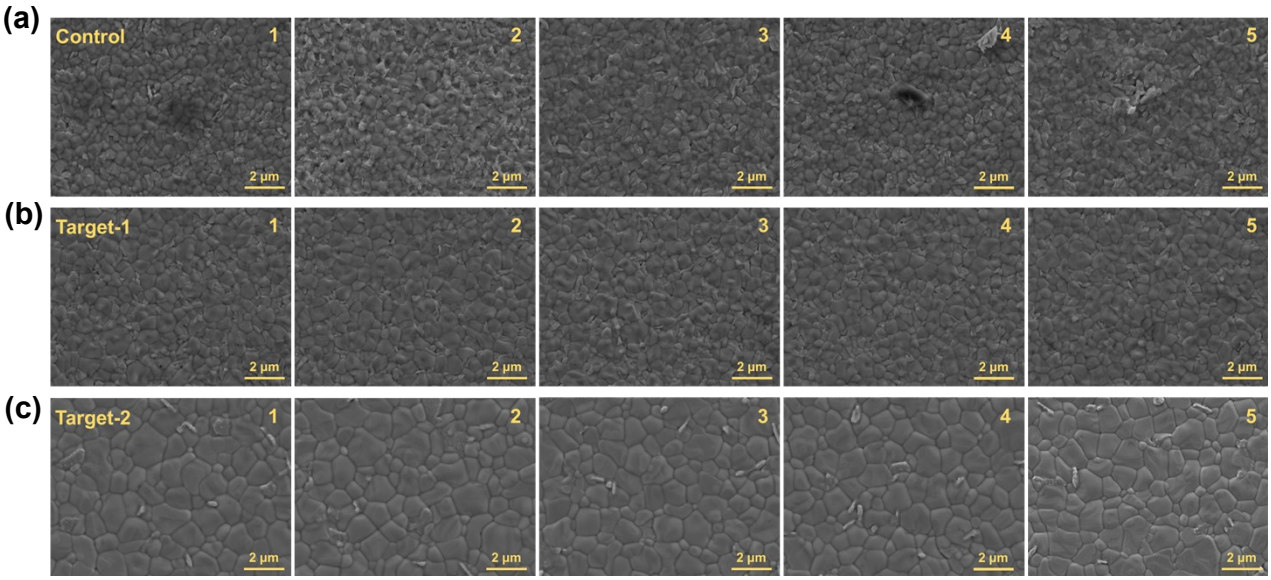

Fig. S28. SEM images of large area (5×5 cm^2) (a) control, (b) target-1 and (c) target-2 perovskite films, which divided into 5 selected pieces (regions 1-5).

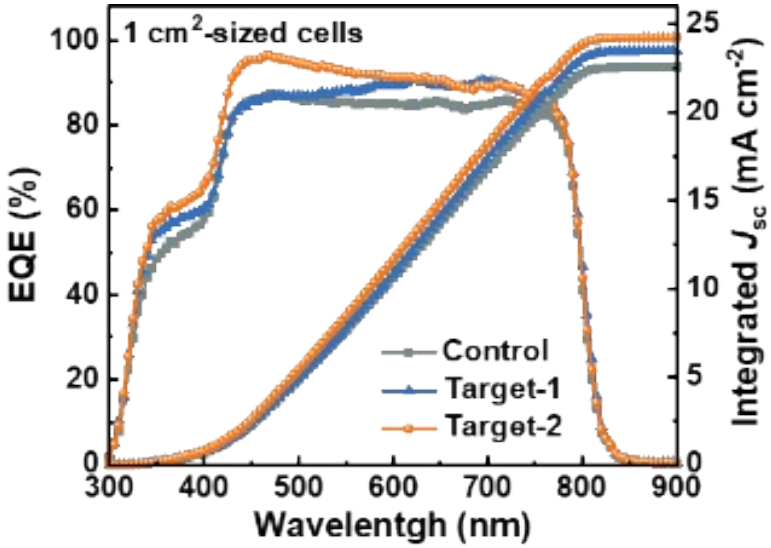

Fig. S29. EQE spectra and integrated photocurrents of 1.01 cm^2 $FAPbI_3$ PVSCs based on control, target-1, and target-2 perovskite layers under AM 1.5G 100 mW/cm^2 illumination.

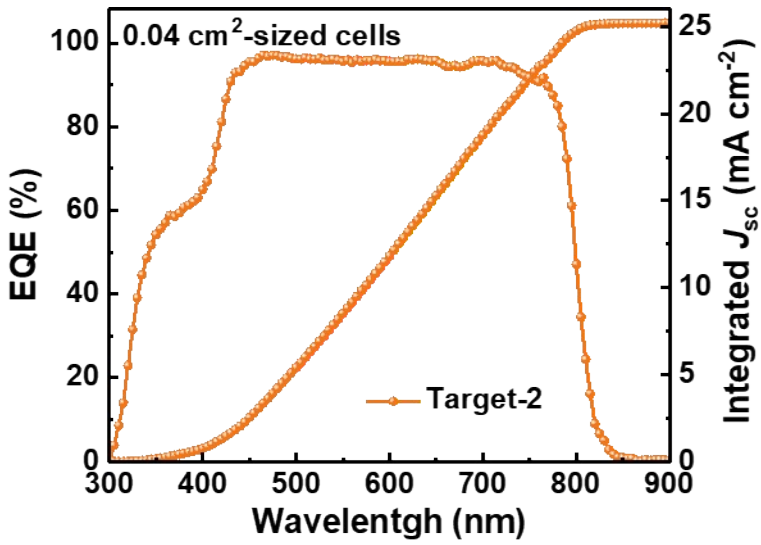

Fig. S30. EQE spectrum and integrated photocurrent of 0.04 cm^2 $FAPbI_3$ PVSC based on target-2 perovskite layer under AM 1.5G 100 mW/cm^2 illumination.

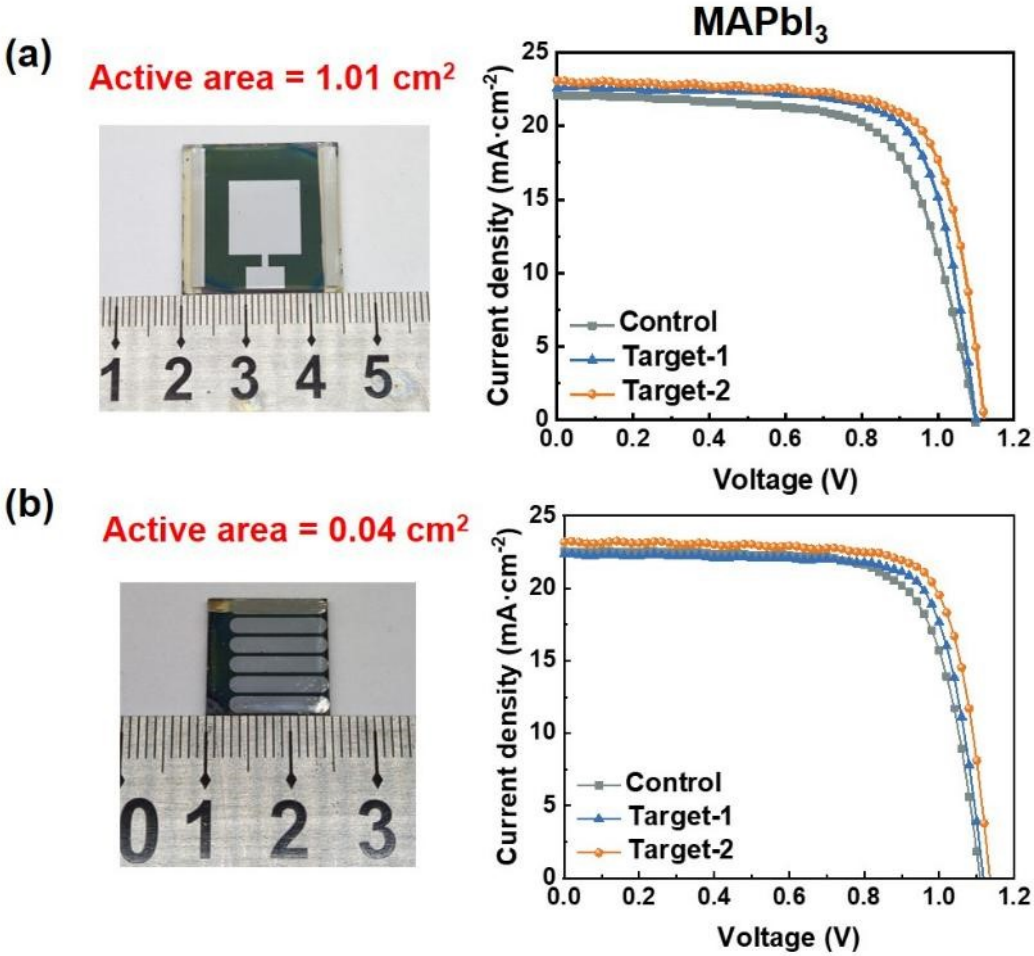

Fig. S31. Photographs and *J-V* curves of (a) centimeter-scale and (b) millimeter-scale $MAPbI_3$ PVSCs based on control, target-1, and target-2 perovskite layers under AM 1.5G 100 mW/cm^2 illumination.

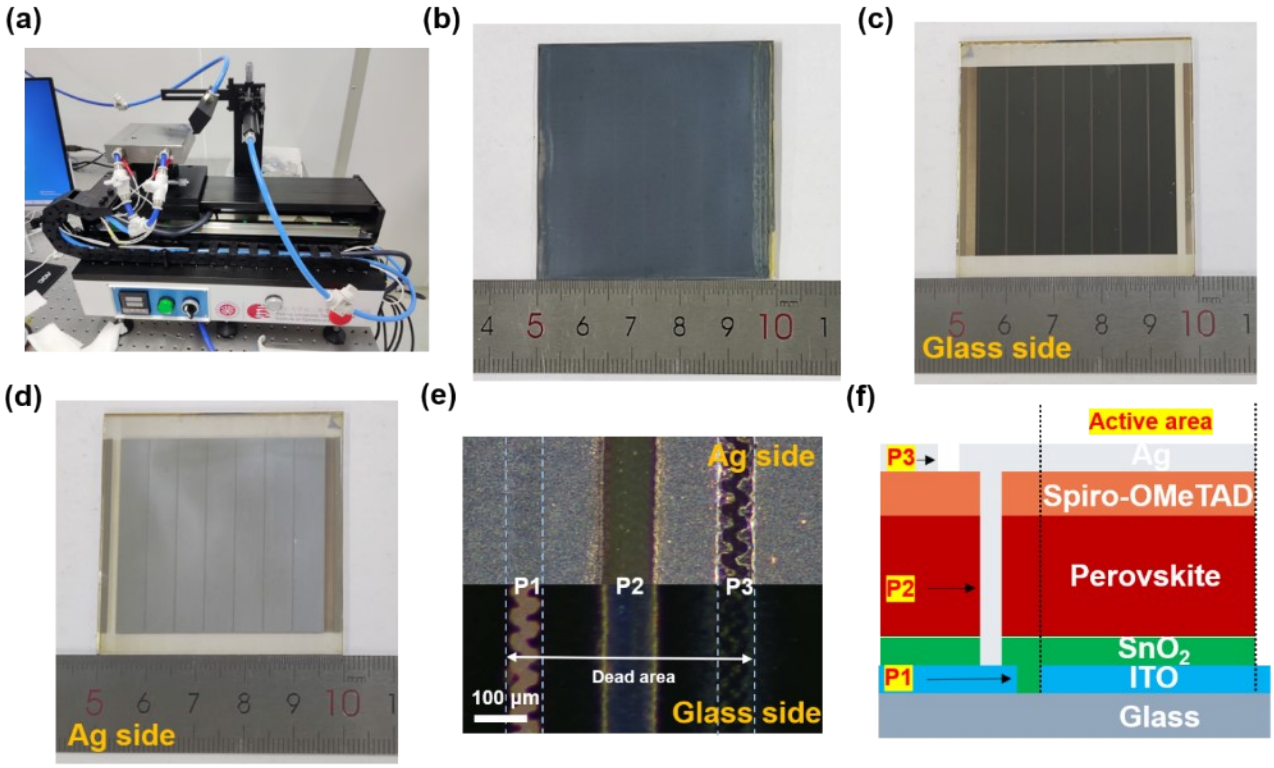

Fig. S32. Photographs of (a) the meniscus blade coating device and (b) 5×5 cm^2 area for target-2 perovskite film. Photographs of 5×5 cm^2 area perovskite solar module for (c) glass side and (d) Ag side. (e) Optical microscopic images of the P1, P2, and P3 etched lines used in module fabrication. (f) Structure schematic of module consists of seven sub-cells connected by laser etching.

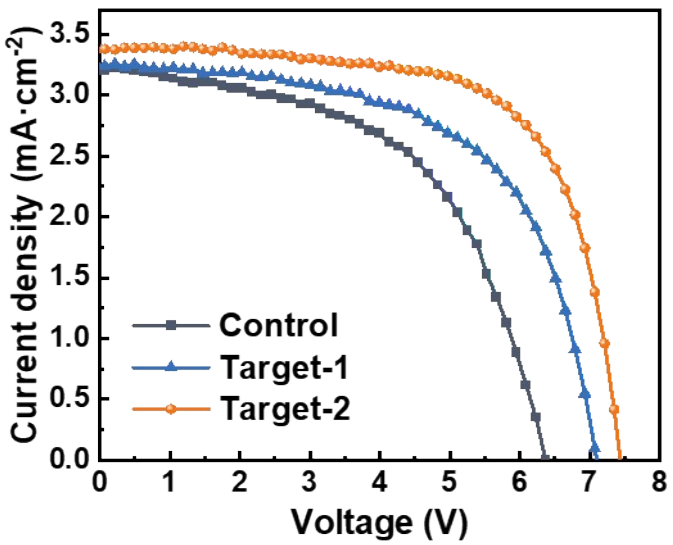

Fig. S33. *J-V* curves of 5×5 cm^2 area perovskite solar modules based on control, target-1, and target-2 perovskite layers.

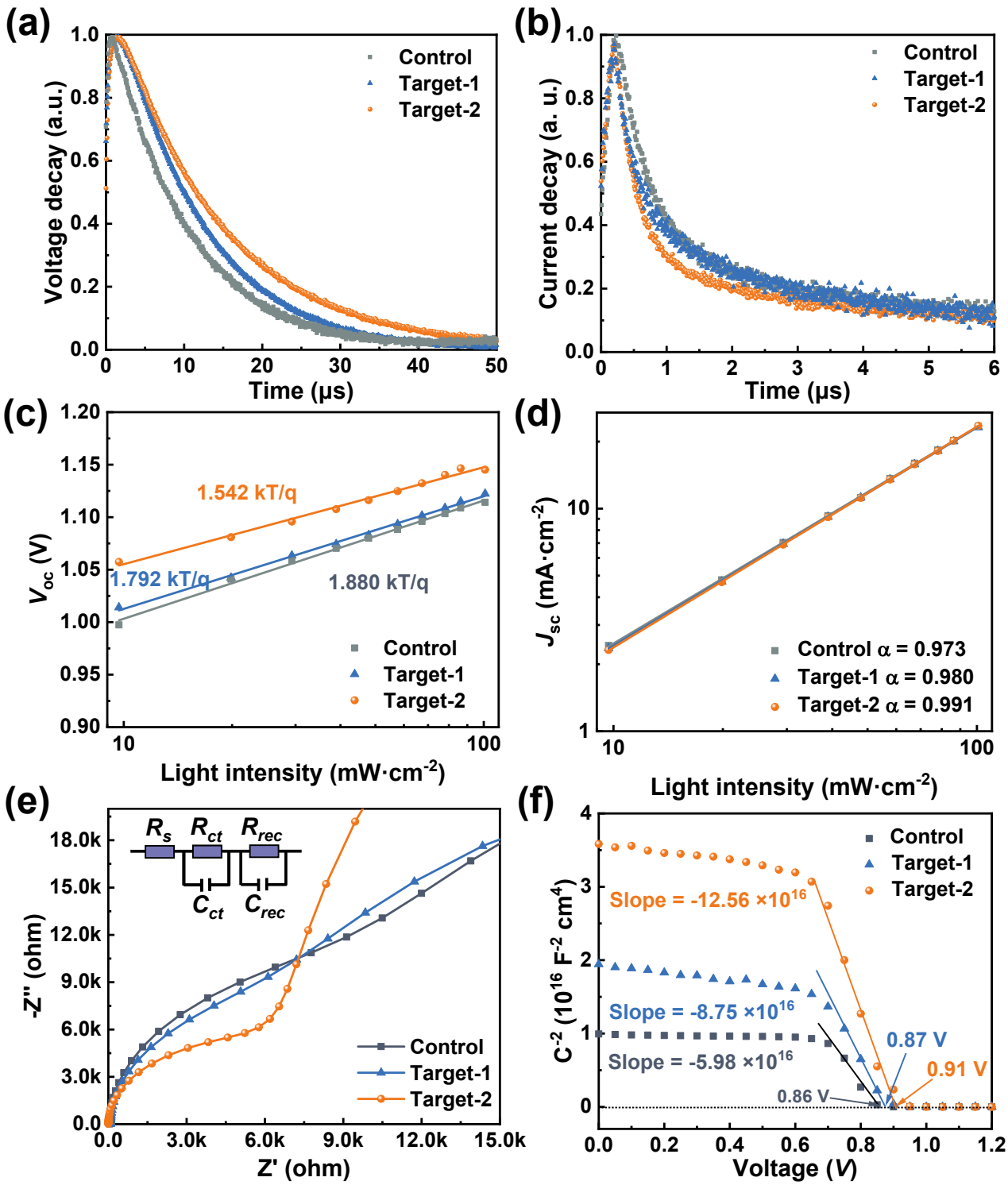

Fig. S34. (a) Transient photovoltage curves, (b) transient photocurrent curves, light intensity dependence of (c) open-circuit voltage (V_{oc}), (d) current density (J_{sc}), (e) Nyquist plots and (f) Mott-Schottky curves of the PVSCs based on control, target-1 and target-2 perovskite layers, respectively.

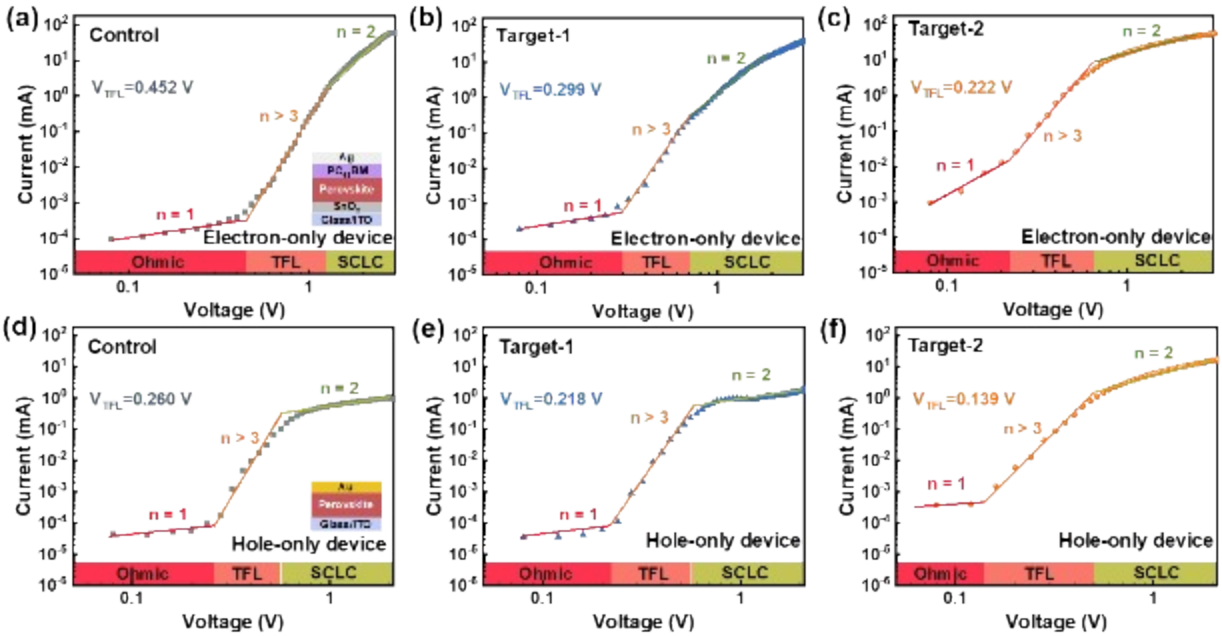

Fig. S35. *J-V* curves for (a-c) the electron-only devices with structure of ITO/SnO_2/perovskite/$PC_{61}BM$/Ag and (d-f) the hole-only devices with the structure of ITO/perovskite/Au based on the space-charge-limited-current (SCLC) model. The formula of SCLC model is $N_t = \frac{2\varepsilon_0\varepsilon_r V_{TFL}}{qL^2}$, where q, L, ε_0, ε_r are elementary charge, the thickness of the perovskite layer, vacuum permittivity (8.85×10^{-12} F·m^{-1}), and relative dielectric constant (46.9).

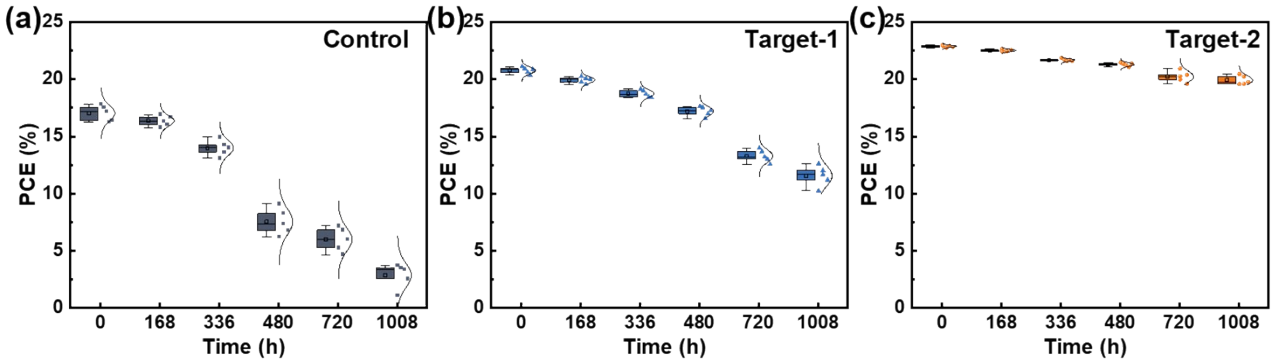

Fig. S36. PCE distribution from decays of the unencapsulated PVSCs under AM 1.5G light soaking in air (25±5 °C, 50±5% RH). 5 devices for each condition represented in the plots.

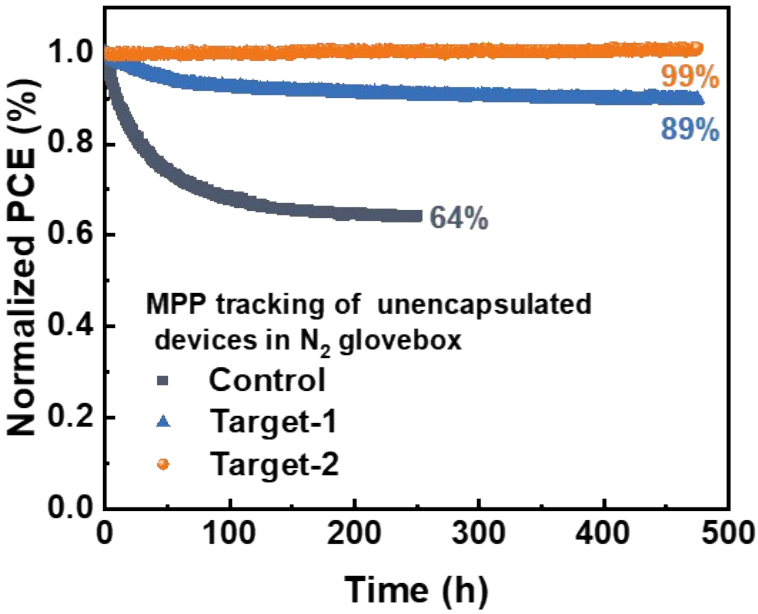

Fig. S37. The Maximum Power Point (MPP) tracking of unencapsulated centimeter-scale PVSCs under continuous light exposure conditions (AM 1.5G, N_2 atmosphere).

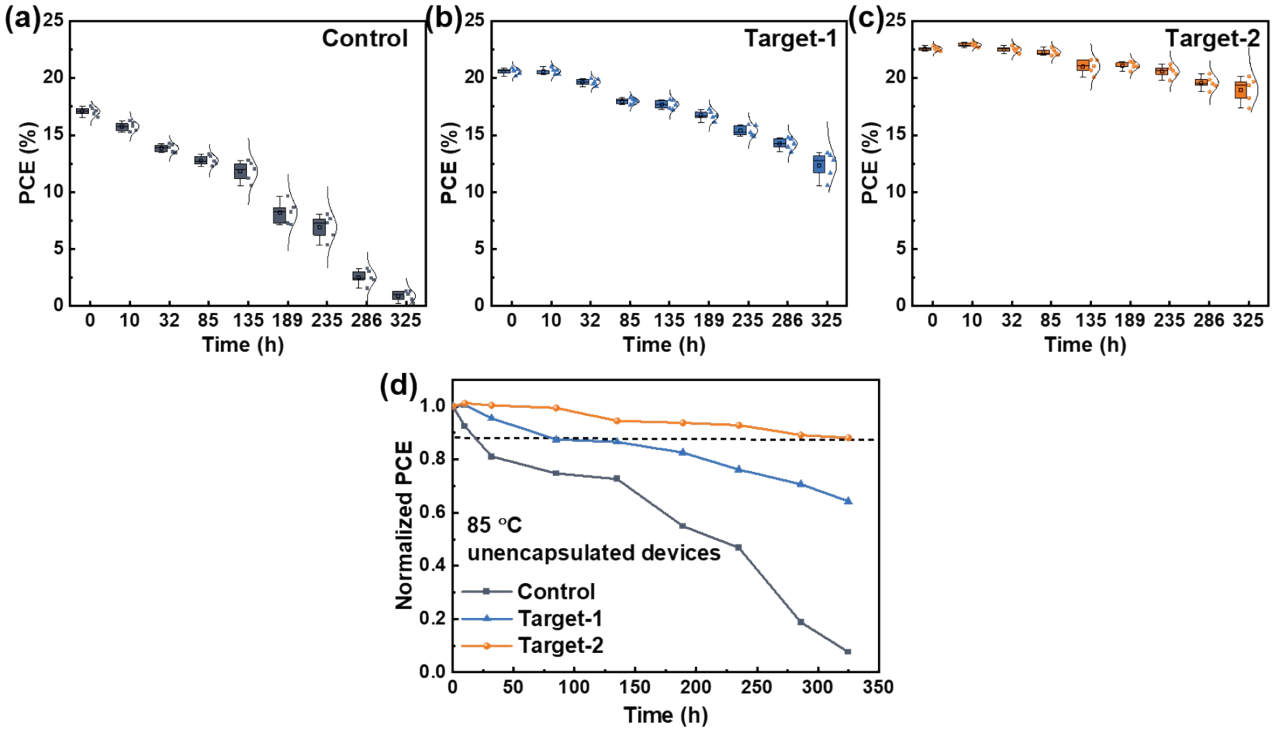

Fig. S38. (a-c) PCE distribution from decays of the PVSCs and corresponding champion PVSC based on control, target-1 and target-2 perovskite exposed in N_2 glove box at 85 °C without any encapsulation. 5 devices for each condition represented in the plots.

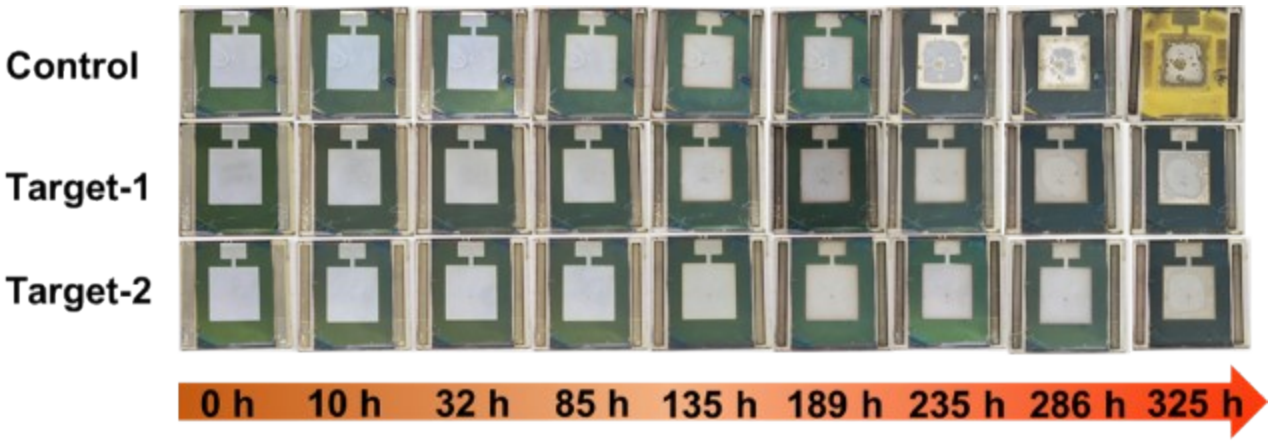

Fig. S39. The photographs of the champion PVSCs based on control, target-1 and target-2 PVSCs exposed in N_2 glove box at 85 °C without any encapsulation.

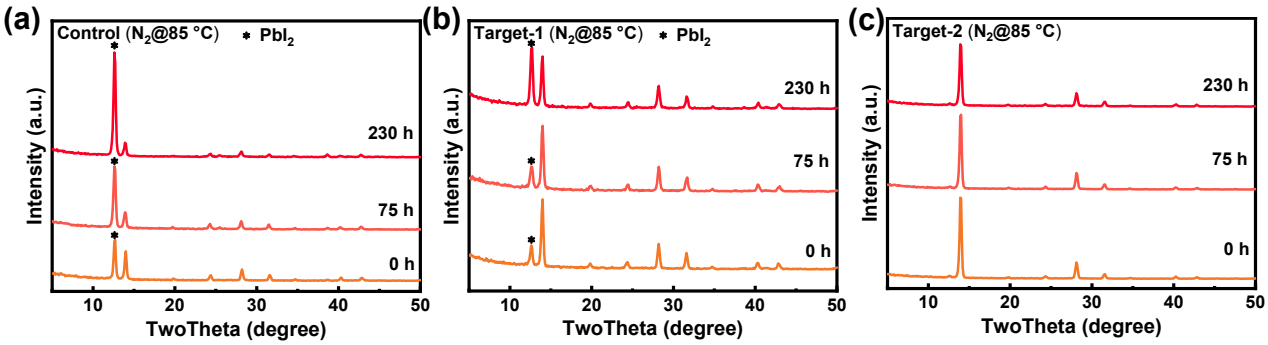

Fig. S40. XRD patterns of control, target-1, and target-2 perovskite films exposed in N_2 glove box at 85 °C for 0 h, 75 h and 230 h.

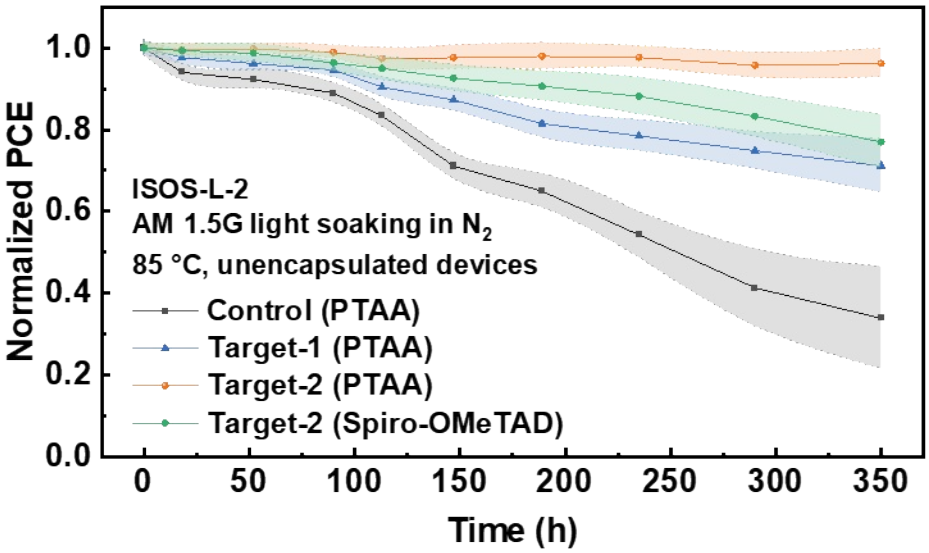

Fig. S41. PCE decays of the unencapsulated centimeter-scale PVSCs exposed at 85 °C under AM 1.5G light soaking in N_2 atmosphere, following ISOS-L-2 standard. The shaded regions represent the standard deviation for 5 devices. The target-2 devices (spiro-OMeTAD as an HTL) preserved 77% of their initial PCE at 85 °C under AM 1.5G light soaking in N_2 atmosphere. The target-2 devices (PTAA as an HTL) exhibited no degradation after 350 h, while control and target-1 devices (PTAA as an HTL) retained only 34% and 71% of their initial performance, respectively.

Table S1. Molecular structures, character, boiling point and vapor pressure of typical solvents and additive used in the PbI_2 precursor inks.

Solvent	**Dimethylformamide (DMF)**	**Dimethyl sulfoxide (DMSO)**	**Dihydrolevoglucosenone (Cyrene)**
Molecular structure	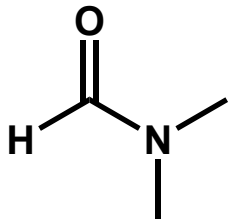	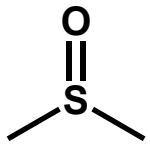	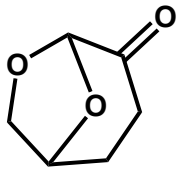
Character (20 °C)	Liquid (volatile)	Liquid (non-volatile)	Liquid (non-volatile)
Boiling point (20 °C)	152-154	189	227
Vapor pressure at 20 °C (Pa)	360	192	-

Table S2. Calculated binding energies for PbI_2·DMF, PbI_2·DMSO, PbI_2·Cyrene, FA^+·DMF, FA^+·DMSO, and FA^+·Cyrene using DFT calculation.

Molecule	Binding energy (eV)
PbI_2·DMF	-0.627
PbI_2·DMSO	-0.675
PbI_2·Cyrene	-1.066
FA^+·DMF	-1.53
FA^+·DMSO	-1.6
FA^+·Cyrene	-1.87

Table S3. Device of PCE and PCE loss of recently reported millimeter-scale and centimeter-scale PVSCs.

Device	Millimeter-scale PCE (Area)	Centimeter-scale PCE (Area)	PCE loss	Ref.
ITO/SnO_2/$FA_xMA_{1-x}PbI_3$/ Spiro-OMeTAD/MoO_3/Ag	24.37% (0.10 cm^2)	22.26% (1.01 cm^2)	8.66%	1
FTO/ZnO/m-TiO_2/ $Cs_{0.05}Rb_{0.05}(FA_{0.83}MA_{0.17})_{0.90}Pb(I_{0.95}Br_{0.05})_3$/Spiro-OMeTAD/Au	24.16% (0.096 cm^2)	22.81% (1.00 cm^2)	5.59%	2
FTO/SnO_2/ $FA_{0.83}Cs_{0.17}PbI_3$ /Spiro-OMeTAD/Au	23.35% (0.148 cm^2)	22.53% (1.0 cm^2)	3.51%	3
FTO/SnO_2/$Cs_{0.05}(FA_{0.95}MA_{0.05})_{0.05}Pb(I_{0.95}Br_{0.05})_3$/Spiro-OMeTAD/Au	24.27% (0.08 cm^2)	23.35% (1.0 cm^2)	3.79%	4
ITO/SnO_2/$Cs_{0.125}(FA_{0.87}MA_{0.13})_{0.875}Pb(I_{0.995}Br_{0.05})_3$/ LD-Perovskite/Spiro-OMeTAD/Au	24.18% (0.049 cm^2)	22.94% (1.0 cm^2)	5.13%	5
ITO/SnO_2/$FA_{0.93}MA_{0.07}PbI_3$ /Spiro-OMeTAD/MoO_x/Ag	24.23% (0.062 cm^2)	22.69% (1.0 cm^2)	7.59%	6
FTO/c-TiO_2/paa-QD-SnO_2/ $FAPbI_3$/Spiro-OMeTAD/Au	25.7% (0.08 cm^2)	23.3% (1.0 cm^2)	9.34%	7
ITO/SnO_2/$Cs_{0.05}FA_{0.95}PbI_3$/HTL/MoO3 /Ag	21.5% (0.09 cm2)	19.5% (1.0 cm^2)	9.30%	8
FTO/c-TiO_2/$FAPbI_3$/Spiro-OMeTAD/Au	22.1% (0.096 cm^2)	19.7% (1 cm^2)	10.86%	9
ITO/PTAA/Perovskite/C60/BCP/Cu	21.5% (0.08 cm^2)	20.0% (1.1 cm^2)	6.98%	10
ITO/SnO_2/$(FAPbI_3)_x(MAPbBr_3)_{1-x}$/Spiro-OMeTAD/Au	21.6% (0.074 cm^2)	20.1% (1 cm^2)	6.94%	11
FTO/c-TiO_2/$FAPbI_3$/DM/Au	23.2% (0.094 cm^2)	20.9% (1 cm^2)	9.91%	12
FTO/c-TiO_2/$FAPbI_3$/Spiro-mF/Au	24.82% (0.082 cm^2)	22.31 (1 cm^2)	10.11%	13
ITO/SnO_2/$FAPbI_3$/ Spiro-OMeTAD/Au	26.07% (0.08 cm^2)	24.63% (1 cm^2)	5.85%	14
ITO/SnO_2/$FA_xMA_{1-x}PbI_3$/ Spiro-OMeTAD/Ag	**24.20% (0.04 cm^2)**	**23.13% (1.01 cm^2)**	**4.4%**	**This work**

Table S4. Photovoltaic parameters of the perovskite solar modules based on control, target-1 and target-2 perovskite layers under standard AM 1.5 G illumination (100 mW·cm^{-2}).

Area	Perovskite		V_{oc} (V)	J_{sc} (mA·cm^{-2})	FF (%)	PCE (%)
Module (16.90 cm^2)	$FAPbI_3$	Control	6.37	3.22	54.38	11.15
		Target-1	7.10	3.25	59.34	13.70
		Target-2	7.44	3.38	67.33	16.90

References

1 T. Zhou, Z. Xu, R. Wang, X. Dong, Q. Fu and Y. Liu, *Adv. Mater.*, 2022, **34**, 2200705.

2 Z. Fang, L. Wang, X. Mu, B. Chen, Q. Xiong, W. D. Wang, J. Ding, P. Gao, Y. Wu and J. Cao, *J. Am. Chem. Soc.*, 2021, **143**, 18989.

3 T. Bu, J. Li, H. Li, C. Tian, J. Su, G. Tong, L. K. Ono, C. Wang, Z. Lin, N. Chai, X.-L. Zhang, J. Chang, J. Lu, J. Zhong, W. Huang, Y. Qi, Y.-B. Cheng and F. Huang, *Science*, 2021, **372**, 1327.

4 N. Li, X. Niu, L. Li, H. Wang, Z. Huang, Y. Zhang, Y. Chen, X. Zhang, C. Zhu, H. Zai, Y. Bai, S. Ma, H. Liu, X. Liu, Z. Guo, G. Liu, R. Fan, H. Chen, J. Wang, Y. Lun, X. Wang, J. Hong, H. Xie, D. S. Jakob, X. G. Xu, Q. Chen and H. Zhou, *Science*, 2021, **373**, 561.

5 J. Chen, Y. Yang, H. Dong, J. Li, X. Zhu, J. Xu, F. Pan, F. Yuan, J. Dai, B. Jiao, X. Hou, A. K.-Y. Jen and Z. Wu, *Sci. Adv.*, 2022, **8**, eabk2722.

6 W. Chen, S. Liu, Q. Li, Q. Cheng, B. He, Z. Hu, Y. Shen, H. Chen, G. Xu, X. Ou, H. Yang, J. Xi, Y. Li and Y. Li, *Adv. Mater.*, 2022, **34**, 2110482.

7 M. Kim, J. Jeong, H. Lu, T. K. Lee, F. T. Eickemeyer, Y. Liu, I. W. Choi, S. J. Choi, Y. Jo, H.-B. Kim, S.-I. Mo, Y.-K. Kim, H. Lee, N. G. An, S. Cho, W. R. Tress, S. M. Zakeeruddin, A. Hagfeldt, J. Y. Kim, M. Grätzel and D. S. Kim, *Science*, 2022, **375**, 302.

8 T. Niu, W. Zhu, Y. Zhang, Q. Xue, X. Jiao, Z. Wang, Y.-M. Xie, P. Li, R. Chen, F. Huang, Y. Li, H.-L. Yip and Y. Cao, *Joule*, 2021, **5**, 249.

9 W. S. Yang, B.-W. Park, E. H. Jung, N. J. Jeon, Y. C. Kim, D. U. Lee, S. S. Shin, J. Seo, E. K. Kim, J. H. Noh and S. I. Seok, *Science*, 2017, **356**, 1376.

10 W.-Q. Wu, Z. Yang, P. N. Rudd, Y. Shao, X. Dai, H. Wei, J. Zhao, Y. Fang, Q. Wang, Y. Liu, Y. Deng, X. Xiao, Y. Feng and J. Huang, *Sci. Adv.*, 2019, **5**, eaav8925.

11 Q. Jiang, Z. Chu, P. Wang, X. Yang, H. Liu, Y. Wang, Z. Yin, J. Wu, X. Zhang and J. You, *Adv. Mater.*, 2017, **29**, 1703852.

12 N. J. Jeon, H. Na, E. H. Jung, T.-Y. Yang, Y. G. Lee, G. Kim, H.-W. Shin, S. Il Seok, J. Lee and J. Seo, *Nat. Energy*, 2018, **3**, 682.

13 M. Jeong, I. W. Choi, E. M. Go, Y. Cho, M. Kim, B. Lee, S. Jeong, Y. Jo, H. W. Choi, J. Lee, J.-H. Bae, S. K. Kwak, D. S. Kim and C. Yang, *Science*, 2020, **369**, 1615.

14 Z. Huang, Y. Bai, X. Huang, J. Li, Y. Wu, Y. Chen, K. Li, X. Niu, N. Li, G. Liu, Y. Zhang, H. Zai, Q. Chen, T. Lei, L. Wang and H. Zhou, *Nature*, 2023, **623**, 531.